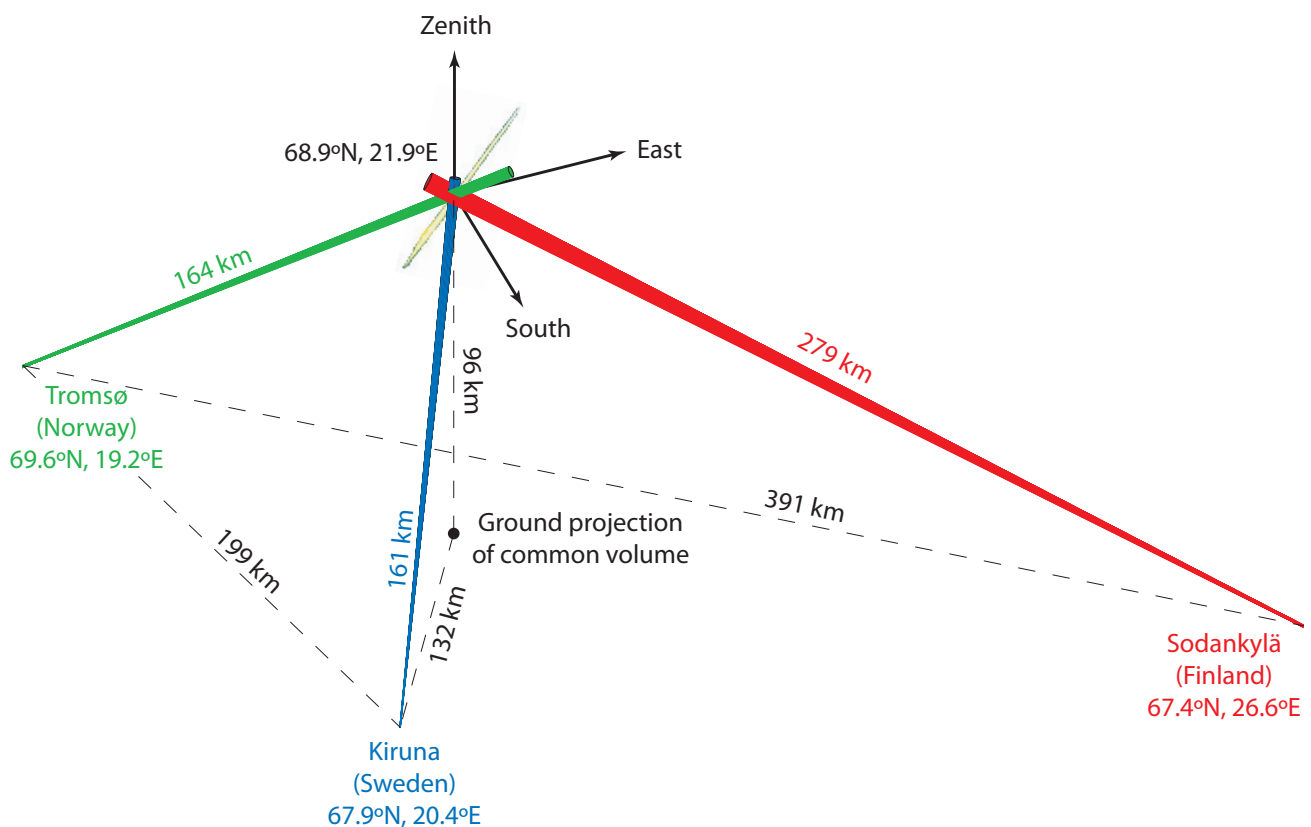


High-resolution meteor exploration with tristatic radar methods

Johan Kero

IRF Scientific Report 293, 2008



INSTITUTET FÖR RYMDFYSIK
Swedish Institute of Space Physics
Kiruna, Sweden

HIGH-RESOLUTION METEOR EXPLORATION WITH TRISTATIC RADAR METHODS

Akademisk avhandling

som med vederbörligt tillstånd av rektorsämbetet vid Umeå universitet
för avläggande av teknologie doktorsexamen i rymdteknik framlägges
till offentlig granskning i IRF:s aula, fredagen den 25 april 2008, kl. 10:00

av

Johan Kero

FAKULTETSOPPONENT

Dr. Sigrid Close, Los Alamos National Laboratory, New Mexico, USA



HIGH-RESOLUTION METEOR EXPLORATION
WITH TRISTATIC RADAR METHODS

Johan Kero

IRF Scientific Report 293

HÖGUPPLÖSTA METEORSTUDIER
MED TRESTATISK RADARTEKNIK



Swedish Institute of Space Physics
Kiruna 2008

Front cover illustration:

Meteor observing geometry of the EISCAT UHF system.
Johan Kero and Csilla Szasz

Back cover photo:

The Sodankylä EISCAT UHF antenna.
Csilla Szasz

©Johan Kero

DOCTORAL THESIS AT THE SWEDISH INSTITUTE OF SPACE PHYSICS
High-resolution meteor exploration with tristatic radar methods

DOKTORSAVHANDLING VID INSTITUTET FÖR RYMDFYSIK
Högupplösta meteorstudier med trestatisk radarteknik

Typeset by Csilla Szasz in \LaTeX .
Kiruna, March 2008

IRF Scientific Report 293
ISSN 0284-1703
ISBN 978-91-977255-3-8

Printed at the Swedish Institute of Space Physics
Box 812
SE-981 28, Kiruna, Sweden
March 2008

HÖGUPPLÖSTA METEORSTUDIER MED TRESTATISK RADARTEKNIK

SAMMANFATTNING

Meteoror är ljusfenomen på natthimlen som i vardagligt tal kallas fallande stjärnor. Ljusstrimmorna alstras av meteoroider, små partiklar på banor genom solsystemet, som kolliderar med jordens atmosfär. Förutom ljus genererar meteoroider regioner av joniserat plasma, som är detekterbara med radar. Meteoriska huvudekon tycks komma från kompakta radarmål på ungefär 100 km höjd och rör sig genom atmosfären med de infallande meteoroidernas hastighet. Huvudekons signalstyrka förefaller oberoende av vinkeln mellan radarmålens rörelseriktning och riktningen från vilken radiovågorna infaller och sprids.

Avhandlingen sammanfattar huvudekoobservationer från fyra 24-timmarsmätningar mellan 2002 och 2005 med det trestatiska 930 MHz EISCAT UHF-radarsystemet och en 6-timmarsmätning under 2003 med den monostatiska 224 MHz EISCAT VHF-radarn. Avhandlingen innehåller den första observationella bekräftelsen på att en meteoroid av sub-millimeterstorlek faller sönder i två distinkta fragment i atmosfären. Upptäckten är betydelsefull för studier av meteoroiders växelverkanprocesser med atmosfären och interplanetärt/interstellärt stofts materialegenskaper.

EISCAT UHF-systemet består av tre vitt åtskilda mottagarstationer, vilket gör det till ett unikt mätinstrument för studier av meteoroiders egenskaper och hur radiovågor sprids från de radarmål som ger upphov till huvudekon. Avhandlingen presenterar en metod med vilken ett radarmåls position kan bestämmas om det detekteras samtidigt med de tre mottagarna. Metoden används till att med hög noggrannhet beräkna meteorers radartvärsnitt samt meteoroiders hastighet och atmosfärsinbromsning. De detekterade huvudekorna genereras av meteoroider med i princip alla av mätgeometrin tillåtna rörelseriktningar i förhållande till radarstrålen, ända ut till 130° från radiovågornas spridningsriktning. Enskilda meteorers radartvärsnitt är likvärdiga inom mät-noggrannheten i de tre mottagarstationernas dataserier, men en svag trend antyder att radartvärsnittet minskar med ökande vinkel mellan meteoroidernas rörelseriktning och spridningsriktningen.

En statistisk utvärdering av mättekniken visar att den uppmätta dopplerhastigheten stämmer överens med radarmålens flygtidshastighet. Detta innebär att dopplerhastigheterna är väntevärdesriktiga och opåverkade av bidrag från det spår av plasma som meteoroiderna lämnar efter sig. De uppmätta hastigheterna är 19-70 km/s, men bara ett fåtal detekterade meteoroider är långsammare än 30 km/s. Meteoroidmassorna är uppskattade till 10^{-9} - $10^{-5.5}$ kg genom jämförelser av observationerna med simuleringar av meteoroiders färd genom atmosfären i en numerisk ablationsmodell.

NYCKELORD: meteoror, meteoroider, interplanetärt stoft, radar, huvudekon, ablation, meteorisk fragmentation

HIGH-RESOLUTION METEOR EXPLORATION WITH TRISTATIC RADAR METHODS

ABSTRACT

A meteor observed with the naked eye is colloquially called a shooting star. The streak of light is generated by an extra-terrestrial particle, a meteoroid, entering the Earth's atmosphere. The term meteor includes both luminosity detectable by optical means and ionization detectable by radar. The radar targets of meteor head echoes have the same motion as the meteoroids on their atmospheric flight and are relatively independent of aspect angle. They appear to be compact regions of plasma created at around 100 km altitude and have no appreciable duration.

This thesis reviews the meteor head echo observations carried out with the tristatic 930 MHz EISCAT UHF radar system during four 24 h runs between 2002 and 2005, and a 6 h run in 2003 with the monostatic 224 MHz EISCAT VHF radar. It contains the first strong observational evidence of a submillimeter-sized meteoroid breaking apart into two distinct fragments. This discovery promises to be useful in the further understanding of the interaction processes of meteoroids with the Earth's atmosphere and thus also the properties of interplanetary/interstellar dust.

The tristatic capability of the EISCAT UHF system makes it a unique tool for investigating the physical properties of meteoroids and the meteor head echo scattering process. The thesis presents a method for determining the position of a compact radar target in the common volume of the antenna beams and demonstrate its applicability for meteor studies. The inferred positions of the meteor targets are used to estimate their velocities, decelerations, directions of arrival and radar cross sections (RCS) with unprecedented accuracy. The head echoes are detected at virtually all possible aspect angles all the way out to 130° from the meteoroid trajectory, limited by the antenna pointing directions. The RCS of individual meteors simultaneously observed with the three receivers are equal within the accuracy of the measurements with a very slight trend suggesting that the RCS decreases with increasing aspect angle.

A statistical evaluation of the measurement technique shows that the determined Doppler velocity agrees with the target range rate. This demonstrates that no contribution from slipping plasma is detected and that the Doppler velocities are unbiased within the measurement accuracy. The velocities of the detected meteoroids are in the range of 19-70 km/s, but with very few detections at velocities below 30 km/s. The thesis compares observations with a numerical single-body ablation model, which simulates the physical processes during meteoroid flight through the atmosphere. The estimated meteoroid masses are in the range of 10^{-9} - $10^{-5.5}$ kg.

KEYWORDS: meteors, meteoroids, interplanetary dust, radar, head echoes, ablation, meteoroid fragmentation

CONTENTS

Sammanfattning	v
Abstract	vii
List of included papers	1
1 Introduction	3
1.1 Dust and meteoroids	4
1.2 Outline	4
2 Meteor echo theory	7
2.1 Early history	7
2.2 Classical theory of radio meteor observations	8
2.3 Underdense and overdense trails	9
2.4 Echo from an underdense trail	10
2.5 Diffusion of underdense trails	11
2.6 Echo from an overdense trail	13
2.7 The meteor head echo	14
2.8 Critical frequency, plasma frequency and resonances	15
3 Ablation model	17
3.1 Input parameters	18
3.2 Atmosphere model MSIS-E-90	18
3.3 Calculation logistics	18
3.4 Mass loss	19
3.4.1 Ablation	19
3.4.2 Sputtering	19
3.5 Flow regime	22
3.6 Deceleration	23
3.7 Meteoroid temperature	24
3.8 Radar cross section	25
3.9 Output parameters	26
3.10 Fit of the model to the data	27
4 Summary of the included papers	31
4.1 Paper I: Determination of meteoroid physical properties from tristatic radar observations	31
4.2 Paper II: On the meteoric head echo radar cross section angular dependence	31
4.3 Paper III: Three dimensional radar observation of a submillimeter meteoroid fragmentation	32
4.4 Paper IV: Power fluctuations in meteor head echoes observed with the EISCAT VHF radar	32
4.5 Paper V: Properties of the meteor head echoes observed with the EISCAT radars	33
4.6 Paper VI: The EISCAT meteor code	33
Acknowledgements/Tillkännagivanden	35
References	37
Papers I–V	43

LIST OF INCLUDED PAPERS

This thesis is based on the work reported in the following papers:

- I. Kero, J., Szasz, C., Pellinen-Wannberg, A., Wannberg, G., Westman, A., and Meisel, D. D. (2008). Determination of meteoroid physical properties from tristatic radar observations, *Annales Geophysicae*, submitted.
- II. Kero, J., Szasz, C., Wannberg, G., Pellinen-Wannberg, A., and Westman, A. (2008). On the meteoric head echo radar cross section angular dependence, *Geophysical Research Letters*, doi:10.1029/2008GL033402.
- III. Kero, J., Szasz, C., Pellinen-Wannberg, A., Wannberg, G., Westman, A., and Meisel, D. D. (2008). Three dimensional radar observation of a submillimeter meteoroid fragmentation, *Geophysical Research Letters*, 35:L04101.
- IV. Kero, J., Szasz, C., Pellinen-Wannberg, A., Wannberg, G., and Westman, A. (2004). Power fluctuations in meteor head echoes observed with the EISCAT VHF radar, *Earth, Moon, and Planets*, 95:633–638.
- V. Kero, J., Szasz, C., Pellinen-Wannberg, A., Wannberg, G., and Westman, A. (2005). Properties of the meteor head echoes observed with the EISCAT radars, *Proceedings of Radio Vetenskap och Kommunikation, Linköping 2005*, pp. 197–200, FOI and Tekniska högskolan Linköpings universitet.
- VI. Wannberg, G., Westman, A., Kero, J., Szasz, C., and Pellinen-Wannberg, A. (2008). The EISCAT meteor code, *Annales Geophysicae*, submitted.

The papers have been reprinted with permission by the publishers, and are included as appendices to this thesis.

1 INTRODUCTION

THE SCIENTIFIC STUDY of meteorites and the discipline of astronomy that deals with meteors is called meteoritics. Even though many of the scrutinized objects are relics from the formation of the solar nebula about 4.5 billion years ago, the field itself is quite a young branch of modern science.

One of the pioneers of this young science was Ernst Chladni (1756-1827), a German physicist. Chladni published a book in 1794, in which he proposed meteorites to be of extraterrestrial origin. This was a very controversial statement at the time and it took almost a decade before the idea won general acceptance. The resistance against the hypothesis was not only due to religious reasons, though there are several examples of meteorites that have been accorded religious significance, but because of the general scientific belief that no small objects exist in interplanetary space (McSween, 1999). Some scientists did not accept the phenomenon of stones falling from the skies at all. Those who did, on the other hand, explained meteorite formation by condensation in clouds or coagulation of ash from erupting volcanos. Rapid improvements in the field of mineral chemistry and the lucky fall of a large stony meteorite from a clear, blue sky into the village of Wold Cottage, England, in 1795 were key events to progress in meteoritics. Samples of the Wold Cottage meteorite were examined by Edward Howard, a British chemist, and Jaques de Bournon, a French mineralogist. They reported their findings of nickel-iron in grains from the stone in 1802. Several forms of grains containing different combinations of these elements, like kamacite and taenite, are abundant in meteorites but are extremely rare in terrestrial rocks (McSween, 1999). Nickel had earlier also been found in iron meteorites and thus provided a chemical link pointing towards a similar, extraterrestrial, origin.

A solar system is born when a core of large enough mass is formed due to gravitational attraction in an interstellar cloud of molecules and dust (Rietmeijer, 2002). As angular momentum is conserved, the dust cloud rotates faster and faster as matter accumulates from the more distant parts of the cloud towards the core. The rotating core will eventually collapse into a protostar with a surrounding disk and eject matter along its rotational axis. The disk-like system becomes a solar nebula, in which planet formation can take place owing to dust accretion processes at different places in the disk.

The lifetime of dust particles in the solar system is of the order of only 10^5 years. The fate of a particle depends primarily on the ratio of the solar radiation pressure force to the gravitational force acting on it, but perturbations due to, e.g., a close encounter with a planet may also play a role (Williams, 2002). If the solar radiation pressure force dominates, the particle eventually escapes the solar system on a hyperbolic path. Otherwise, it slowly spirals inwards due to the Poynting-Robertson effect and is finally destroyed by the heat of the Sun. The Poynting-Robertson effect is the loss of momentum caused by absorption of solar radiation in a frame that is stationary with respect to the Sun and reemission in a frame stationary with respect to an orbiting body (Poynting, 1903; Robertson, 1937). Sub-micron-sized and smaller particles escape on hyperbolic trajectories; the upper size limit depends on particle material properties.

Hypervelocity microimpact craters on larger grains of meteoritic and lunar origin attest that dust has existed in interplanetary space for billions of years (Brownlee, 1985). This implies that new dust is created continuously. All solid bodies in the solar system can release material during impact events. As impact events large enough for releasing

particulates from planets have been rare, at least during the second half of the lifetime of the solar system, comets and asteroids are the main sources of dust. When active comets approach perihelion they produce dust and meteoroids via ice sublimation. Asteroids can only generate dust through collisions.

1.1 Dust and meteoroids

There are several definitions of dust particles and meteoroids. Some authors classify cosmic dust as being “particulate material that exists or has existed in the interplanetary medium as bodies smaller than 1 mm” (Brownlee, 1985). Authors in the field of meteor physics usually prefer a lower upper size limit, as particles < 1 mm in diameter are able to produce observable meteors.

The term meteor has developed from referring only to the luminosity produced in the interaction processes of an extra-terrestrial particle with the Earth atmosphere, seen visually as a shooting star, to include all meteoric phenomena detectable by optical means or with radar (Beech and Steel, 1995). It is therefore quite common to state the method of observation implicitly, e.g., visual meteor, photographic meteor, telescopic meteor or radio meteor. The observable quantities are the essence of the term meteor and should therefore be used to redefine the present definition of a meteoroid used by the International Astronomical Union (IAU): “a solid object moving in interplanetary space, of a size considerably smaller than an asteroid and considerably larger than an atom or a molecule” (Millman, 1961).

The criteria for producing a detectable meteor is in principle governed by the way a meteoroid loses energy after entering a planetary atmosphere. The meteoroid mass loss processes are collectively referred to as ablation. Mass is lost through thermal processes like vaporization and fusion of molten material, but also via fragmentation as well as sputtering of single atoms knocked out from the meteoroid by the impact of high-speed atmospheric constituents (Öpik, 1958; Bronshten, 1983). However, due to their high area over mass ratios, particles smaller than ~ 100 μm lose their energy mainly in form of radiation rather than ablation. Therefore, dust particles produce very small amounts of light and ionization. Research groups using the world’s most sensitive radar facility, the Arecibo Observatory 430 MHz UHF radar (AO) in Puerto Rico, claim to be able to detect the ionization produced by particles as small as $\simeq 1$ μm (Janches et al., 2001).

1.2 Outline

This thesis discusses meteor head echo observations conducted with the VHF and UHF radar systems of the European Incoherent Scatter Scientific Association (EISCAT). Section 2 contains an overview of radar observations of meteors, starting with their origin in ionospheric physics in the 1930s and rapid development during the advent of radar astronomy after World War II. Ionization trail formation and specular meteor trail observations are discussed to quite a large extent in Section 2.2 to 2.6. The purpose is to introduce meteor physics, radar observations and general concepts not included in the appended research papers, which exclusively report meteor head echo observations. A meteor head echo comes from a compact region of plasma close to and travelling along with a meteoroid at a velocity of tens of km/s, discussed in Section 2.7. A meteor trail echo is the reflection from the slowly drifting column of plasma left behind the meteoroid. Meteor trail observations with radar are treated in full detail by McKinley (1961) and references therein. An extensive review of the history of radar astronomy is given by Butrica (1996).

Section 3 describes a numerical single-body ablation model with which the observations are compared in order to estimate the meteoroid masses at detection as well as their atmospheric entry properties (mass, velocity, etc.). The ablation model is ultimately based on work summarized in the standard textbooks on meteor physics by (Öpik, 1958) and Bronshten (1983). Murad and Williams (2002) give a comprehensive review of some of the most important advances in observational techniques and physics of meteoroid ablation subsequent to these.

The included research papers are summarized in Section 4.

2 METEOR ECHO THEORY

A METEOROID travelling through the atmosphere leaves a wake train of ions and electrons behind. The enhancement in ionization can be detected by radar systems in many different ways. This chapter summarises the characteristics of different kinds of observed echoes and the mechanisms likely to cause them. Two different geometries of specular meteor trail radars are treated (forward- and backscatter systems) as well as observations of meteor head echoes.

2.1 Early history

Nagaoka (1929) was the first to note the coincidence between the ionospheric E-layer (at that time referred to as the Kennelly-Heaviside layer) and the determined altitude of visual meteors. Skellett (1931) hypothesised the ionizing effect of meteoroids entering the Earth's atmosphere and its possible impact on radio wave propagation in the upper atmosphere. This thought originated from a study of transatlantic short-wave telephone circuits (Butrica, 1996). Observations of momentary ionospheric echoes from irregular heights were reported from the British radio measurements carried out during the Second International Polar Year 1932-33 by Appleton et al. (1937), and also by Eckersley (1937), who used commercial equipment. Skellett (1938) and others further investigated and strongly supported the notion that all, or at least some, of these echoes were caused by meteors.

During World War II, gun-laying radars were adopted to detect rockets entering British airspace (Butrica, 1996). However, many alarms turned out to be false. The task of investigating why was laid upon James S. Hey, who associated them with meteors. Hey and Stewart (1946) reported investigations of short duration scatter echo measurements using army equipment and simultaneous sightings of visual meteors. There were about seven times as many radio echoes as visual observations. Hey and Stewart also established a method to determine meteor stream radiants by using three stations with radar beams aimed in different directions and by assuming that the reflections came from columns of ionized gas with maximum radar cross section (RCS) at 90° aspect angle.

Hey et al. (1947) intensified these efforts during the Giacobinid meteor shower of 1946 and noticed that a faint fast-moving echo could sometimes be discerned prior to the main, presumably specular, echo. Thus they concluded that "The approaching meteor first presents a weak echoing source due to the ionization close to it. It leaves a column of ionization behind it, but since this is initially straight it cannot give a return reflection until it approaches the point of intersection of the normal from the observing station to the ionized column". They used the relation between range (R) and time (t) of the approaching targets to calculate their velocity by assuming that they approached the radar along trajectories describes by

$$R^2 = R_0^2 + v^2 (t - t_0)^2, \quad (1)$$

where R_0 and t_0 are the values at the specular point. The computed velocities of 22 meteoroids are consistent with the geocentric velocity of the Giacobinid stream derived

using other methods. The full half-power beam width of the employed radar system was 32° . It is not clear whether any meteor echoes were observed from meteoroids travelling on trajectories further than a beam width away from the perpendicular direction to the boresight axis and consequently not giving rise to specular scattering. They may deliberately have rejected such echoes because of their altogether faint character or been prevented from observing strongly Doppler shifted echoes due to receiver hardware limitations.

After the war systematic scientific radar investigations of meteors were commenced all around the world. In Britain, the greatest efforts were assembled at the Jodrell Bank Experimental station in Manchester (Lovell, 1947; Butrica, 1996). Correlated visual, photographic and radar observations were initiated, e.g., by the National Research Council of Canada and the Dominion Observatory in Ottawa (Millman et al., 1947). In the USA, a radar meteor project under the direction of Fred Whipple was initiated at the Harvard College Observatory in 1957 (Butrica, 1996). Efforts to improve the meteor radar techniques originally developed at Jodrell Bank were later on carried out within in the NASA meteor research program by Cook et al. (1972) and others at the Smithsonian Astrophysical Observatory.

The first international meteor symposium at which ideas and information gathered with various observational methods were presented was organized at Jodrell Bank in July 1954 (Kaiser, 1955). The counterpart today is the international meteoroids conference organized every third year, most recently by the Institut d'Estudis Espacials de Catalunya (Institute for Space Studies of Catalonia) in Barcelona, Spain, in 2007. A comprehensive and interdisciplinary view on modern meteor science was assembled at the meteoroids 2004 conference by Hawkes et al. (2005).

2.2 Classical theory of radio meteor observations

Meteor patrol radars are optimized to detect meteor trails through specular reflection. With a specular meteor radar system, such as the commercially available SKiYMET (Hocking et al., 2001), it is possible to detect hundreds of meteors per hour as the beam of transmitted radio waves is very wide and enables detection in virtually all directions from the radar. A low-power radar transmitter is enough for good statistics. A multi-station receiver system such as the Advanced Meteor Orbit Radar (AMOR) in New Zealand (Baggaley et al., 1994) or the Canadian Meteor Orbit Radar (CMOR) in Ontario (Jones et al., 2005) enables orbit determination of detected meteors.

In a backscatter system, where the transmitter and the receiver are collocated, the requirement of specular reflection means that to be detected, the meteor trail must be perpendicular to the radar beam.

The conditions for meteor detection with a forward scattering system are illustrated in Figure 1. The meteoroid propagates along a path (M). To be detected, M must be tangential to an arbitrary ellipsoid with the transmitter (TX) and receiver (RX) in its two foci, and the point of tangency (p) must lie within the meteor zone. If the meteoroid passes the beam under any other geometrical condition within the meteor zone the transmitted radio waves will still be reflected, but not to the receiver. For simplicity, only a vertical cross-section of the ellipsoid (E) is drawn in Figure 1. In this context the meteor zone is the region of the atmosphere in which the propagating meteoroid produces enhanced ionization detectable by radar. Most detections appear within a limited interval at an altitude of 80–120 km.

Both AMOR and CMOR consist of three forward-scatter receiver arrays situated a few kilometres apart along two baselines. The three receiver arrays often detect time-shifted specular reflections from the same meteor. The shift in time of the specular condition and the interferometric capabilities of each receiver array enables meteoroid velocity computation (Webster et al., 2004).

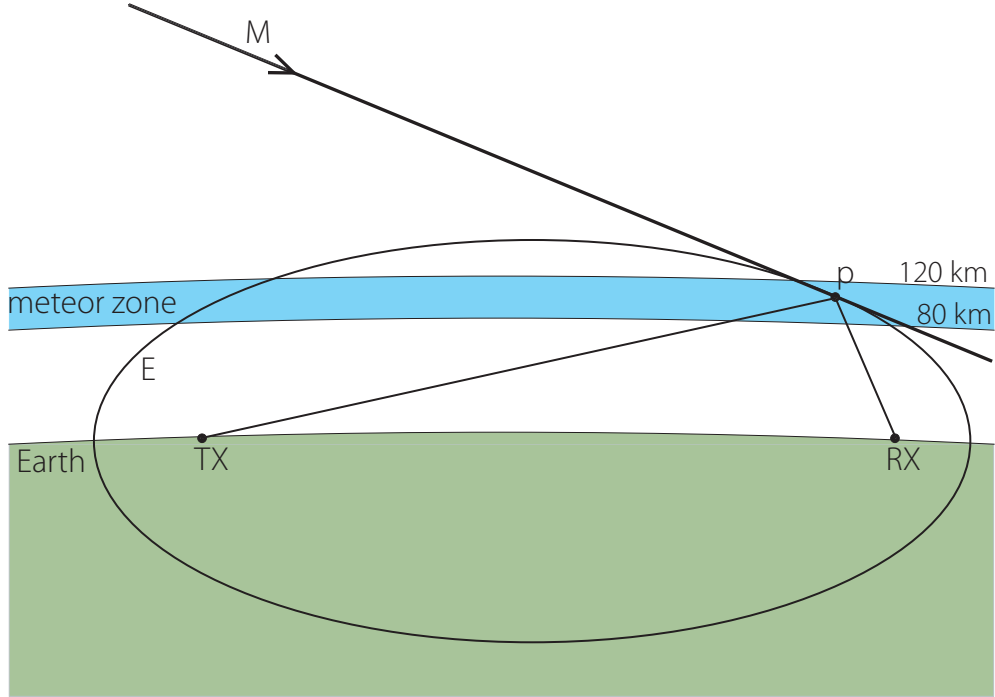


Figure 1: The forward scatter geometry of a meteor detection.

2.3 Underdense and overdense trails

In classical meteor radar terminology, trails are classified as underdense or overdense, depending on the volume density of electrons in the wake train. If the density is sufficiently low, radio waves can penetrate the trail and scattering occurs independently from the free electrons within the trail (Blackett and Lovell, 1941; Lovell and Clegg, 1948). If the density is large enough, secondary scattering from electron to electron becomes important. Hence the electrons no longer behave as independent scatterers and the incident wave cannot penetrate the column freely. The dielectric constant (κ) of an ionized gas differs from the vacuum value of unity due to the number of electrons per m^3 (N) according to

$$\kappa = 1 - \frac{N\lambda^2}{\pi} r_e \approx 1 - 81 \frac{N}{f^2}, \quad (2)$$

where λ is the wavelength of the incident radiation (m), f the corresponding frequency (Hz) and $r_e = e^2 / (e_0 m_0 c^2) \approx 2.8 \cdot 10^{-15}$ m the electron radius. A trail is defined as overdense when $\kappa < 0$ throughout an appreciable volume of the ionized gas, which means that the radio waves are reflected from the surface of the meteor trail as from a metallic surface. At commonly-used meteor radar frequencies of 30 – 50 MHz, this happens if the initial electron line density¹ exceeds $\sim 10^{14} \text{ m}^{-1}$ (McKinley, 1961). The axial dielectric constant can, however, be highly negative in the centre of an underdense trail without resulting in total reflection; the transition from underdense to overdense scattering is not distinct.

To facilitate automated meteor analysis algorithms, overdense echoes are routinely removed, e.g., in the AMOR data set (Galligan and Baggaley, 2004), as their properties are different from those of underdense echoes.

¹The line density is the radially integrated trail electron density.

2.4 Echo from an underdense trail

Each free electron in an underdense trail scatters the incident wave independently and the signal received by a radar system is the sum of the contributions from all individual electrons. The power received due to scattering off one electron in a backscatter system can be derived from the radar equation (McKinley, 1961)

$$\Delta P_R = \frac{P_T G_T}{4\pi R^2} \cdot \frac{\sigma_{eff}}{4\pi R^2} \cdot \frac{G_R \lambda^2}{4\pi} = \frac{P_T G_T G_R \lambda^2 \sigma_{eff}}{64\pi^3 R^4}, \quad (3)$$

where

- P_T = transmitted power,
- G_T = transmitter antenna gain,
- G_R = receiver antenna gain,
- σ_{eff} = electron cross section, $4\pi r_e \approx 1 \cdot 10^{-28} \text{ m}^2$,
- R = distance between the transmitter/receiver and the scatter point,
- $\frac{P_T G_T}{4\pi R^2}$ = power flux (W/m^2) of the incident wave at a distance R ,
- $\frac{\sigma_{eff}}{4\pi R^2}$ = the part of the scattered power available at the receiver, and
- $\frac{G_R \lambda^2}{4\pi}$ = effective absorbing area of the receiver antenna.

To summarise the contributions from all available electrons, the trail is approximated by a line density of q electrons per meter of path. When dealing with a sum of waves, care has to be taken to account for the difference in phase between contributions from different parts of the trail. For this reason the integration over the length of the trail has to be done with the amplitude of the field vectors, rather than the power flux, as integrand. The phase of the received wave from different sections of the trail at time t will depend on the range R (i.e. wave distance $2R$) as $\sin(2\pi(ft_1 - 2R/\lambda))$. The peak amplitude due to scattering of one electron is $(2\mathbf{r}\Delta P_R)^{1/2}$, where \mathbf{r} is the receiver input impedance. The total field received due to scattering off all electrons between two arbitrary points s_1 and s along the trail can in turn be expressed as

$$E = (2\mathbf{r}\Delta P_R)^{1/2} \cdot \int_{s_1}^s q \sin\left(2\pi\left(ft_1 - \frac{2R}{\lambda}\right)\right) ds. \quad (4)$$

Two assumptions are made to evaluate the integral: q is considered constant along the trail and the range R is approximated by $R \simeq R_0 + s^2/2R_0$. The latter is illustrated in Figure 2. Equation (4) can under these assumptions be restructured by introducing two variable transformations, $\chi = 2\pi(ft - 2R_0/\lambda)$ and $2s = x(R_0\lambda)^{1/2}$. When parameters that are constant along the path of integration are taken outside the integral sign, we get

$$E = \frac{(2\mathbf{r}\Delta P_R R_0 \lambda)^{1/2}}{2} \cdot q \cdot \int_{x_1}^x \sin\left(\chi - \frac{\pi x^2}{2}\right) dx. \quad (5)$$

This can be rewritten with the help of the trigonometric identity

$$\sin\left(\chi - \frac{\pi x^2}{2}\right) = \sin \chi \cdot \cos \frac{\pi x^2}{2} - \cos \chi \cdot \sin \frac{\pi x^2}{2}, \quad (6)$$

and the Fresnel integrals

$$\mathbf{C} = \int_{x_1}^x \cos \frac{\pi x^2}{2} dx \quad \text{and} \quad \mathbf{S} = \int_{x_1}^x \sin \frac{\pi x^2}{2} dx \quad (7)$$

to

$$E = \frac{(2\mathbf{r}\Delta P_R R_0 \lambda)^{1/2}}{2} \cdot q \cdot (\mathbf{C} \sin \chi - \mathbf{S} \cos \chi). \quad (8)$$

The Fresnel integrals vary much less with time than the radio frequency (f) does and, consequently, the parameter χ . As the expression $\mathbf{C} \sin \chi - \mathbf{S} \cos \chi$ can be rewritten as $-\sqrt{\mathbf{C}^2 + \mathbf{S}^2} \cdot \cos(\chi - \arctan(\mathbf{C}/\mathbf{S}))$ and the quasi-instantaneous power (P_R) received from all trail electrons is found by taking a time average over an interval that is short compared to the fluctuation period of the Fresnel integrals, P_R is found to be

$$P_R = \frac{E^2}{2\mathbf{r}} = \frac{\Delta P_R R_0 \lambda}{2} \left(\frac{\mathbf{C}^2 + \mathbf{S}^2}{2} \right) q^2. \quad (9)$$

Using the definition of the power ΔP_R , received due to scattering off one electron in Equation (3) and the result of Equation (9),

$$\begin{aligned} P_R &= \frac{P_T G_T G_R \lambda^3 \sigma_{eff}}{128 \pi^3 R_0^3} \left(\frac{\mathbf{C}^2 + \mathbf{S}^2}{2} \right) q^2 \\ &\simeq 2.5 \cdot 10^{-32} P_T G_T G_R \left(\frac{\lambda}{R_0} \right)^3 \left(\frac{\mathbf{C}^2 + \mathbf{S}^2}{2} \right) q^2. \end{aligned} \quad (10)$$

The expression inside the brackets of Equation (10) can be deduced from the Cornu spiral, widely used in diffractive optics, and has a value of unity when evaluated with $s \in (-\infty, \infty)$. In Figure 2, the meteor trail is divided into white and black portions, each corresponding to a Fresnel zone. The phase of the scattered wave front at the receiver varies less than $\pm\pi/2$ within one such zone. For large $|s|$, the approximation $R \simeq R_0 + s^2/2R_0$ will not hold. However, the approximation is valid within the first Fresnel zone, centered around t_0 , which is the main contributor to the total power as illustrated in Figure 2. The received radio echo power reaches a maximum when the meteoroid has passed this first zone. The power then oscillates since contributions from every other Fresnel zone are out of phase. This is apparent from the Cornu Spiral or tables of the Fresnel integrals \mathbf{C} and \mathbf{S} in any elementary text book in optics, e.g., Pedrotti and Pedrotti (1996).

One way to determine the speed (V) of a meteoroid is to measure the time $\Delta\tau_{mn}$ between the m th and n th cycles of the radio echo oscillation described above and compute

$$V = \sqrt{R_0 \lambda} \frac{\sqrt{n} - \sqrt{m}}{\Delta\tau_{mn}}. \quad (11)$$

Another way to estimate the speed of the meteoroid is to measure the echo rise-time t_r , defined as the elapsed time from the echo to ascend from $1/e$ of its maximum value to the actual maximum, and compute

$$V \simeq \frac{e}{2} \cdot \frac{\sqrt{R_0 \lambda}}{2 t_r}. \quad (12)$$

2.5 Diffusion of underdense trails

In the simple theoretical model of an underdense meteor trail echo described in Section 2.4 it is assumed that the trail can be described as a line density of electrons. In reality, the trail consists of Gaussian-like electron and ion density distributions which expand radially (McKinley, 1961). The radial expansion proceeds at a velocity proportional to the local thermal velocity and the ablated meteoric atoms are slowed down by multiple collisions with atmospheric atoms. A few milliseconds after the meteoroid passage, a trail with a finite radius will have formed. The radius is defined as the radial distance at which the electron density has decreased to a factor of $1/e$ times the central

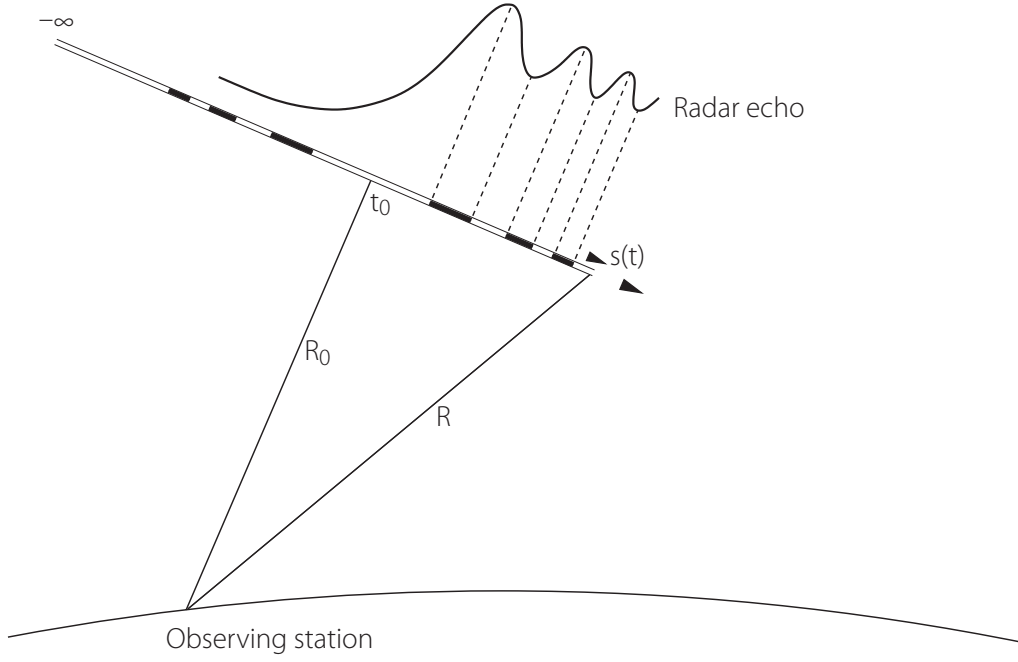


Figure 2: A meteor trail giving rise to Fresnel oscillations, as observed with a backscatter meteor radar. The consecutive Fresnel zones are white if they are in phase with the first zone and black if they are out of phase.

density. This radius is called the initial radius (r_0), and is according to Bronshten (1983) approximately equal to

$$r_0 \simeq 2.58 \cdot 10^{12} \cdot \frac{\mu_a V^{0.8}}{\rho_a}, \quad (13)$$

where μ_a is the mean mass of atmospheric atoms and ρ_a is the atmospheric mass density.

Another estimate of the initial radius is 14 ionic or 3 neutral mean free paths (Manning, 1958). This quantity ranges from about 3 cm at 85 km height to about 2 m at 115 km. If the initial radius is of the same order as the radar wavelength, the echo is strongly attenuated due to the loss of phase coherence between the scattered waves at different radial depths of the trail. The zone where meteors are detectable is therefore limited upwards. The highest level is usually called the underdense echo ceiling. The height of this upper boundary level decreases with increasing radar frequency.

The speed of diffusion of meteoric ions and electrons after the initial radius is formed is determined by the ambipolar diffusion coefficient (D_a), which can be estimated as

$$D_a \simeq 10^{0.067H-5.6} \text{ m}^2/\text{s} \quad (14)$$

at meteoric heights, where $80 \text{ km} < H < 120 \text{ km}$ (McKinley, 1961). The radius (r) of the Gaussian trail increases with time (t) as

$$r = \sqrt{r_0^2 + 4 D_a t}. \quad (15)$$

The expression for P_R in Equation (10), derived under the assumption of a line density of electrons, is attenuated due to the finite radius. To derive an expression for the attenuation, the trail can be treated as a cylinder with shells of different electron densities. When integrating over the trail cross section, McKinley (1961) finds that the received power ($P_{att}(t)$) decreases exponentially with time as

$$P_{att}(t) = P_R \cdot e^{-(8\pi^2 r^2 / \lambda^2)} = P_R \cdot e^{-(8\pi^2 r_0^2 / \lambda^2)} \cdot e^{-(32\pi^2 D_a t / \lambda^2)}. \quad (16)$$

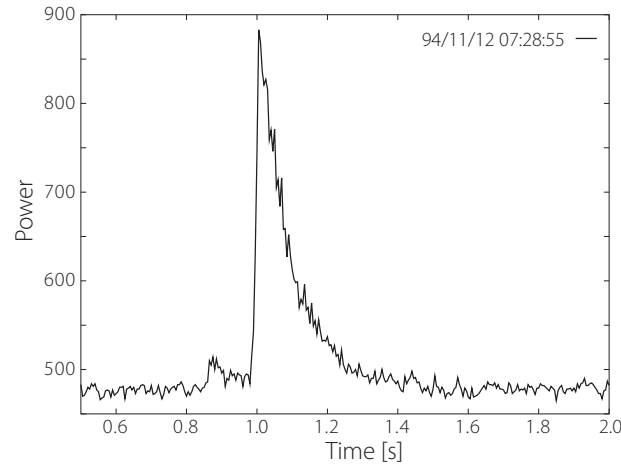


Figure 3: A typical underdense meteoric echo recorded by RAMSES. The vertical axis shows power in an arbitrary unit and the horizontal axis shows time in seconds. The figure is adopted from Wislez (1995).

The first exponential factor in Equation (16), $e^{-(8\pi^2 r_0^2/\lambda^2)}$, is the decrease due to the initial radius when compared to a line density. The second factor, $e^{-(32\pi^2 D_{at}/\lambda^2)}$, represents the decay of the echo with time. The decay time of meteoric echoes is systematically used to determine the ambipolar diffusion coefficient in the atmosphere. The illustrative radar echo presented in Figure 2 shows how the received power profile would look without the effect of diffusion taken into account. In a real power echo profile, the power decreases exponentially with time due to ambipolar diffusion. An example is shown in Figure 3, where the Fresnel oscillations are still discernable. This power profile has been measured with RAMSES (Radio Meteor Survey, Extended System) at the Urania Public Observatory, Hove, Belgium (Wislez, 1995).

The dissipation of meteoric trails is not only influenced by diffusion. The duration of very long-lived echoes is controlled by recombination of electrons with positive ions and attachment of electrons to neutral atoms or molecules, effects that are negligible for short-lived echoes where diffusion processes are strong. Turbulence and wind shear mould long-lived trails, which make meteors good as tracers of atmospheric motion.

2.6 Echo from an overdense trail

When a conventional meteor radar is used, overdense scattering occurs if the initial electron line density of a trail is $\gtrsim 10^{14} \text{ m}^{-1}$ (Section 2.3). Radio waves are scattered from an overdense trail as from a cylindrical, metallic surface. This behaviour is caused by the central part of the trail being so dense that the incident radio waves cannot penetrate it. The scattering solution for an overdense meteor trail was first proposed by Pierce (1938). If the radius of the scattering cylinder is larger than the radio wavelength, the power scattered in the normal direction is proportional to the cylinder radius. This is only a coarse approximation; the high density core of the trail is surrounded by regions of lower density, where the underdense model is valid. Ambipolar diffusion increases the radii of overdense trails (as was described for underdense trails in Section 2.5). Consequently, the electron density in the trail decreases. This leads to a slow rise of the echo strength as long as the volume electron density is still high enough to produce a negative dielectric constant κ (see Equation (2)). The radius of the overdense cylinder

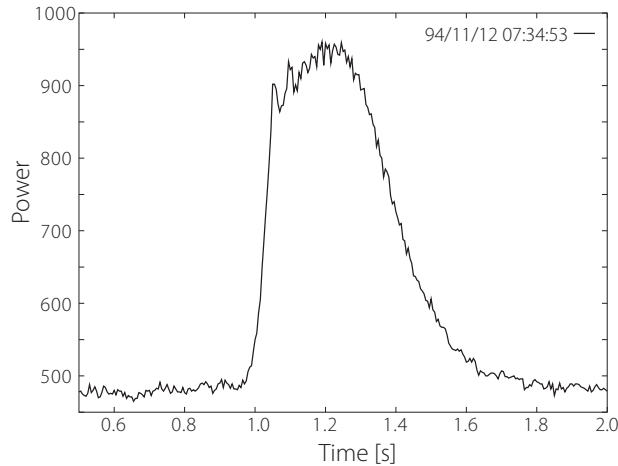


Figure 4: A short overdense meteoric echo. The vertical axis shows power in an arbitrary unit and the horizontal axis shows time in seconds. The figure is adopted from Wislez (1995).

within the trail shrinks until overdense scattering fails and a large underdense trail is all that is left. Figure 4 displays a typical profile of a short overdense echo followed by the exponential decay of the remaining underdense trail recorded by RAMSES (Wislez, 1995).

2.7 The meteor head echo

A meteor head echo has been defined by McKinley and Millman (1949) as “a moving echo having no appreciable enduring characteristics, and with a range-time motion apparently corresponding to the geocentric velocity of the meteoroid”. Echoes of this kind were first reported by Hey et al. (1947) and were subsequently reviewed by McKinley and Millman who described the head echo targets as compact regions of plasma, co-moving with the meteoroids and relatively independent of aspect. Evans (1965, 1966) conducted the first head echo measurements with what today is termed a High Power Large Aperture (HPLA) radar. He used the 440 MHz Millstone Hill radar, which has an operating frequency about an order of magnitude higher than classical specular meteor trail radar systems. Evans observed much smaller radar cross section (RCS) than had been observed at longer wavelengths (McIntosh, 1963). This led him to the conclusion that he had observed something different from previously-reported head echoes. Since the 1990s, meteor head echo observations have been conducted with most HPLA radar facilities around the world (Pellinen-Wannberg and Wannberg, 1994; Mathews et al., 1997; Close et al., 2000; Sato et al., 2000; Chau and Woodman, 2004; Mathews et al., 2008). Differences in the measurement results from the various radar systems indicate that the head echo RCS depend strongly on wavelength (Close et al., 2002).

Jones and Webster (1991) have analyzed meteor head echoes observed with the 33 MHz radar at the Springhill Meteor Observatory. The azimuthal symmetry of the detected meteors are consistent with the assumption of an isotropic reflection process. The same conclusion was drawn by Close et al. (2002), who investigated the polarization ratio of the head echoes detected at 160 MHz and 422 MHz with ALTAIR (Advanced Research Projects Agency Long-Range Tracking and Instrumentation Radar). The polarization ratio they obtained was high regardless of detection altitude, RCS or aspect angle, a result consistent with spherical targets. Paper II in this thesis presents an in-

vestigation of the meteor head echo RCS measured at three different scattering angles simultaneously with the EISCAT UHF system. Meteors are observed at virtually all possible aspect angles all the way out to 130° from the direction of meteoroid propagation, limited by the antenna-pointing directions relative to the local horizon. The monostatic RCS of a meteor target detected in Tromsø is consistent with the simultaneously-probed bistatic RCSs in Kiruna and Sodankylä at different aspect angles. There is a very weak trend suggesting that the RCS may decrease at a rate of 0.2 dB per 10° with increasing aspect angle, which is in quite satisfactory agreement with the plasma and electromagnetic simulations of meteor head echoes performed by Dyrud et al. (2007). The head echo scattering process is still an open issue, but a comprehensive understanding of it is crucial to make full use of the vast volume of observational data, e.g., for global mass influx estimations (Janches et al., 2006).

Different scattering mechanisms have been proposed to render the meteor head echo. Close et al. (2004) have performed the most advanced analytical modelling effort of the meteor head echo to date with a full-wave approach. Close (2004) describes the model in detail.

Wannberg et al. (1996) found that EISCAT VHF and UHF observations can be accounted for by assuming an overdense scattering mechanism. In this formulation the radar target is considered to be a perfectly-conducting sphere of plasma with a radius equal to the radius of the isocontour surface where the plasma density drops below critical. The volume around the meteoroid in which this condition is fulfilled is for sub-millimeter particles estimated to be a few cm wide and for which the RCS is the same as for an ideal Rayleigh target of corresponding size.

Mathews et al. (1997) and Close (2004) point out a flaw of the overdense scattering assumption for the head echo case. It is the small size of the target: an electromagnetic wave incident on a plasma will always penetrate it to some depth. The range of this evanescent wave (the skin depth) into a uniform plasma of critical density is proportional to the wavelength. It is hence argued that overdense scattering as was described by Wannberg et al. (1996) cannot occur for targets that are smaller than the radar wavelength. While this statement is certainly true for uniform density targets, it is not clear what the plasma density profile in the immediate vicinity of a meteoroid looks like.

Mathews et al. (1997) and Mathews (2004) interpret the Arecibo Observatory 430 MHz UHF radar (AO) meteor head echo observations using an underdense scattering mechanism. Mathews et al. assume that each electron scatters independently and hence that the radar target can be considered as a coherent ensemble of N electrons with a total backscattering cross-section of

$$\sigma_{BS} = 4\pi N^2 r_e^2, \quad (17)$$

where r_e is the classical electron radius. While the underdense condition is fulfilled in many faint radio meteor trails, it is unlikely to be valid in the direct vicinity of the meteoroid where the primary ionization takes place and before the initial expansion of the trail.

2.8 Critical frequency, plasma frequency and resonances

The critical frequency obtained from Equation (2) when $\kappa = 0$ refers originally to the plane wave with lowest frequency (f) that can penetrate a deep homogeneous layer of plasma with density N (Herlofson, 1951). The so-defined critical frequency happens to be equal to the plasma frequency of an infinite layer of plasma. It is important to note, however, that the plasma frequency is dependent on the geometrical shape of the system containing the plasma and not only the charge density. Tonks (1931) derived the plasma frequency for an ionized cylinder. The additional inertia associated with the electric field outside the cylindrical plasma reduces the force on each electron to one half

of the infinite layer value. In practice, this result means that the plasma frequency of a cylindrical shape is determined by $\kappa = -1$ and is thus equal to one half of the ordinary infinite layer plasma frequency. The electric field outside a spherical plasma is even greater and the plasma frequency is determined by $\kappa = -2$ (Herlofson, 1951). Hence the plasma frequency is reduced to one third of the infinite layer value.

Herlofson (1951) showed that plasma resonance effects are likely to occur if the probing radar frequency is close to the plasma frequency of the charge distribution in a meteor trail. Resonance occurs for transversally-polarized scattering only, i.e., when the polarization of the electric field is perpendicular to the trail axis, and not for parallel polarization. Meteor trail plasma resonance effects were verified observationally by, e.g., Clegg and Closs (1951) and investigated in detail by Billam and Browne (1956), Greenhow and Neufeld (1956) and others. Billam and Browne showed that the maximum ratio of the amplitude reflection coefficient for transverse polarization to parallel polarization approaches a value of four.

McKinley (1961) concluded that the possible presence of resonance is rarely a significant source of error in measurements of trail decay times and Fresnel velocity estimations. It is, however, of interest for meteor burst communication systems (Wei et al., 1989). A larger number of faint meteor trails can be used to establish communication links if the radio systems are tuned to send messages with a polarization optimized for maximum reflectivity.

Recent numerical simulations by Dyrud et al. (2008) investigate the effect of plasma resonance on meteor head echoes. For radar frequencies near the plasma frequency, large fluctuations occur in the simulated RCS as a function of frequency. This is likely to be one reason why data sets from different radars are difficult to incorporate into one single consistent scattering model.

3 ABLATION MODEL

WE HAVE implemented a single-object ablation model with which to compare our observations. The model is similar to Rogers et al. (2005) and references therein, originally based on Öpik (1958), Bronshten (1983) and Love and Brownlee (1991) with a sputtering model (Section 3.4.2) added as described by Tielens et al. (1994). The input meteoroid parameters to the model are above-atmosphere velocity, mass, density and zenith distance and are further described in Section 3.1. MSIS-E-90 (Hedin, 1991) is used for atmospheric densities, see Section 3.2 for further details.

The tristatic EISCAT UHF data provide precise particle deceleration and RCS (Paper I and II), which are compared and fitted to the ablation model by adjusting the input parameters propagated down through the atmosphere to the observation altitude using a fifth order Runge-Kutta numerical integration technique with a variable step size (Danby, 1988). Four different meteoroid densities (ρ_m), 0.3 g/cc for porous, 1 g/cc for cometary, 3.3 g/cc for asteroidal and 7.8 g/cc for iron material, were paired with mean molecular mass (μ) of ablated vapour of 20 u for graphite (both porous and cometary material), 50 u for silicon dioxide and 56 u for iron respectively (Tielens et al., 1994; Rogers et al., 2005). Every pair of density and molecular mass was propagated down through the atmosphere using every one of five different heat transfer coefficients (Λ) of constant values, 0.2, 0.4, 0.6, 0.8, and 1. Each combination was fitted to the data by iteratively adjusting the input parameters and minimizing the least-square difference between model and measurements. Then the best of the fits was chosen and its input values used as estimates for the extra-atmospheric properties of the meteoroid, as described in Section 3.10. Thus we obtain extra-atmospheric properties of all observed meteoroids and can determine their magnitude (Szasz et al., 2008b), orbits (Szasz et al., 2008a), etc. The mass distribution found by this method is similar to the one reported for the ALTAIR radar data by Close et al. (2007).

The meteoroids are integrated down through the atmosphere to the height of the observation one by one and the starting conditions are changed depending on the fit to the measured data until the fit is optimized. The sections to come describe how the model works and how the fit to the observed parameters is done. If not stated otherwise, all calculations are performed in SI units. Therefore, the dimensions of the parameters are not always specified.

A spherical meteoroid is assumed in all calculations, thus the corresponding shape factor (A) used is 1.21 (Bronshten, 1983). It is further assumed that the meteoroid is propagating through the atmosphere in the free molecular flow regime (Section 3.5). This is a common assumption for submillimeter particles above 96 km altitude (Love and Brownlee, 1991; Campbell-Brown and Koschny, 2004). Previous statistical estimations of EISCAT meteoroid sizes (Pellinen-Wannberg et al., 1998) as well as the present ablation modelling results, reported in Paper I in this thesis and by Szasz et al. (2008b,a), indicate that the particles are small enough for the assumption to be valid.

Fragmentation is not taken into account in the ablation model. If a meteoroid has broken up into pieces before or during the observation, the measured deceleration represents the largest remaining fragment (Ceplecha et al., 1998). This leads to an underestimated atmospheric entry mass. In an event with two dominant fragments, the observed Doppler velocity is proportional to a weighted arithmetic mean of their Doppler velocities, with weights equal to the square root of their RCSs. The received power, and

thus the RCS, may in this case be modulated with a beat frequency proportional to the difference between their Doppler velocities (Paper III).

3.1 Input parameters

The ablation model requires a set of input parameters. The experiment/meteor specific ones are day and hour when the meteor was detected, height of the observation (h_{obs}), and the measured zenith distance (zd) and velocity (v) at the common volume.

The meteoroid density (ρ_m) and heat transfer coefficient (Λ) have been varied between runs to see which values give the best fit to the data.

A set of parameters defining the start and stop conditions for each model run are meteoroid mass (m) or radius (r_m)², starting height (H) for the integration downwards (we have used 500 km for results presented in this thesis) and the greatest tolerable truncation error (TL) defining the variable step size in the integration scheme. If a particle when integrated downwards happens to be very long-lived, the integration process is stopped when either the mass, the height or the velocity reaches limiting values $m_i \leq stop_m \cdot m$, $h_i \leq stop_h$ or $v_i \leq stop_v$ respectively, where m_i , h_i and v_i are the meteoroid mass, height and velocity at step number i . This procedure is further described in Section 3.3.

3.2 Atmosphere model MSIS-E-90

We have used the MSIS-E-90 atmosphere model (Hedin, 1991), which is based on data from sounding rockets, incoherent scatter radar and satellites for densities of atmospheric constituents.

Different atmospheric data was used for every full hour for the days of observation and the number densities were interpolated in height with a polynomial technique using piecewise cubic hermite interpolation to get representative values at any altitude. The interpolations were done only in height, not in time as it was assumed that the values should be fairly constant during one hour. The time of detection is rounded to the closest full hour, for which the values are used. The atmospheric parameters given by the MSIS-E-90 are the number densities O/cm³, N₂/cm³, O₂/cm³, He/cm³, Ar/cm³, H/cm³, N/cm³, and the total mass density, ρ_a (g⁻¹ cm⁻³).

3.3 Calculation logistics

The integration scheme starts at the top of the atmosphere. We have chosen 500 km as the starting altitude and by using a fifth order Runge-Kutta numerical integration technique with a variable step size (Danby, 1988) we have propagated each particle down to the altitude of the observation. One of the integrated parameters is the range to the meteoroid along the meteoroid trajectory (s) from an origin defined as the point at which all three EISCAT UHF antennae were directed, hereafter referred to as the centre of the common volume. (Geometry details are given in Paper I.) The other integrated parameters are meteoroid velocity (v), mass (m), and temperature (T). Only these four parameters are saved at each step in the calculation. All other parameters, determined at each step or not, are recalculated after the particle has been propagated down through the atmosphere (Section 3.9).

²assuming the particles to be spheres, m and r_m are related through: $m = \frac{4}{3}\pi r_m^3 \rho_m$

The measured meteoroid deceleration as well as the measured RCS are compared with the velocity and RCS profiles obtained from the ablation model at the observing altitude. The starting conditions are changed and the integration rerun. This is done until the best least squares fit to the data is found and is repeated with all four meteoroid densities and all five heat transfer coefficients that we have chosen to take into account. Then, the best fits from all pairs of densities and heat transfer coefficients are compared and the run that best fits the data is chosen and its input values used as estimates for the atmospheric entry properties of the meteoroid. Section 3.10 discusses the fitting procedure in more detail. The described procedure is repeated for all trisatic meteor events which contain enough data points for time-of-flight velocity calculations to be compared to the Doppler velocity measurements, a total number of 410 (Table 1 in Paper I).

3.4 Mass loss

Two meteoroid mass loss mechanisms are implemented in the model, thermal ablation and physical sputtering. Once both of them have been determined the total mass loss is the sum of the two results.

3.4.1 Ablation

Ablation is the mass loss of meteoroids due to vaporization, fusion of molten material and fragmentation (Bronshten, 1983). This model does not take fragmentation into account. The calculation procedures in this section are adopted from Rogers et al. (2005) and Hill et al. (2005) (and references within these papers). Thermal ablation is determined from the saturated vapour pressure of the thermally ablated meteoroid material (P_v) given by the Claussius-Clapeyron equation

$$P_v = 10^{C_A - \frac{C_B}{T}}. \quad (18)$$

It should be noted that Equation (18) gives the saturated vapour pressure in units of d/cm², where a dyne is 10⁻⁵ N, and needs to be transformed into SI units. We have adopted the Claussius-Clapeyron coefficients used by Öpik (1958): $C_A = 10.6$ for all meteoric material and $C_B = 13\,500$ K for porous, cometary, and asteroidal material and $C_B = 16\,120$ K for iron material.

Knowing the saturated vapour pressure of the thermally-ablated meteoroid material, the mass loss due to thermal ablation is given by

$$\text{thermal ablation} = \left. \frac{dm}{dt} \right|_{th} = -4A \left(\frac{m}{\rho_m} \right)^{\frac{2}{3}} P_v \sqrt{\frac{\mu}{2\pi kT}}, \quad (19)$$

where μ is the mean molecular mass of the ablated vapour (which depends on the meteoroid density, see Table 1), k is the Boltzmann constant and T is the meteoroid temperature as calculated in the previous step of the integration.

3.4.2 Sputtering

Single atoms knocked out from a solid or liquid substance due to the impact of high-speed atomic particles is called sputtering. Sputtering may, in contrast to thermal ablation, cause meteoroid mass loss in the upper part of the atmosphere before significant heating has taken place, as it does not depend on temperature to any great extent (Öpik, 1958). When implemented in our numerical model similarly to Rogers et al.

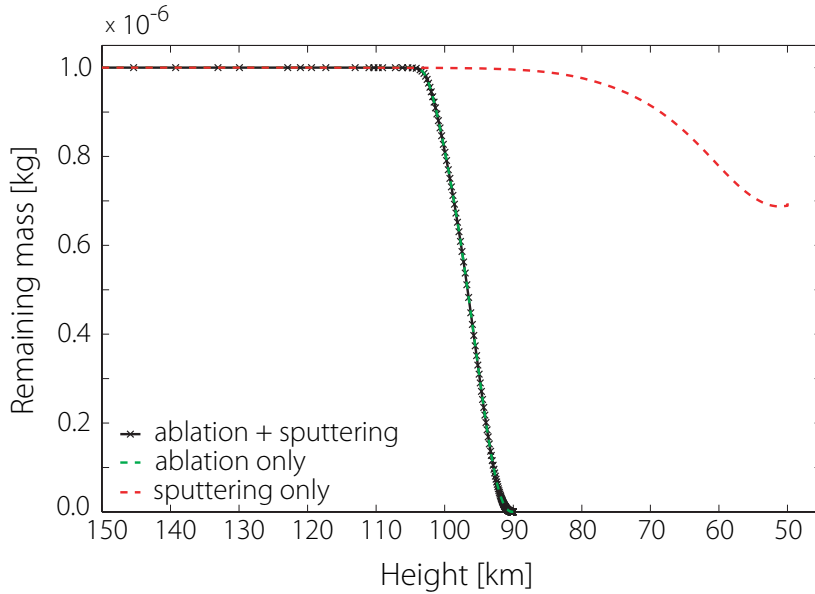


Figure 5: Remaining meteoroid mass when only ablation (green curve), only sputtering (red curve), or both ablation and sputtering (black curve and crosses) are taken into account for a 1×10^{-6} kg test particle with a density of 3.3×10^3 kg/m³. The velocity and zenith distance at the height of the common volume have been set to 60 km/s and 35°, respectively.

Table 1: Meteoroid material characteristics used in sputtering calculations: mass density ρ_m (g/cc), mean atomic mass μ (u), surface binding energy E_B (eV), the “truly” free parameter K which depends on the target material, and the average atomic number Z , both dimensionless. The values are adopted from Tielens et al. (1994) and Öpik (1958).

Meteoroid material	Composition	ρ_m (g/cc)	μ (u)	E_B (eV)	K	Z
Porous	C	0.3	12	4	0.65	6
Cometary	C	1.0	12	4	0.65	6
Asteroidal	SiO ₂	3.3	20	6.4	0.1	10
Iron	Fe	7.8	56	4.1	0.35	26

(2005) and Tielens et al. (1994), sputtering does not significantly influence the meteoroid mass compared to thermal ablation. In Figure 5, the remaining mass of a test particle is plotted versus height if only sputtering, only ablation or both mechanisms are taken into account. It is evident from the figure that sputtering is of minor importance for the mass loss compared to the thermal ablation.

When we compare the atmospheric number densities used in the sputtering calculations by Rogers et al. (2005) to number densities for the same atmospheric constituents given by the MSIS-E-90 model, it is obvious that Rogers et al. (2005) have used incorrect number density values. Their values are a factor of 100 larger than those given by MSIS-E-90. Thus sputtering is a much less important disintegration process than presented in the study and cannot cause significant light production at high altitude as argued in an interrelated paper by Hill et al. (2004), based on the same calculations. The approach they have used in their calculations, however, is good, and we have been guided by it in our implementation of sputtering.

Physical sputtering is a chain reaction induced by particles hitting a target surface. The impinging particles collide with surface atoms, which will in turn collide with other atoms in their vicinity, starting a sequence of collisions. Some of the atoms will reach

Table 2: Characteristics of atmospheric constituents needed for sputtering calculations: mean atomic mass μ_a in u and the average atomic number Z_a .

Molecule	O	N ₂	O ₂	He	Ar	H	N
μ_a (u)	15.9994	14.007	15.999	4.0026	39.948	1.0079	14.007
Z_a	8	7	8	2	18	1	7

the target surface and if they then have enough energy to overcome the potential barrier of the surface, they will escape. The energy needed for a particle to escape is called the surface binding energy (E_B). Thus an atom will be ejected if its velocity component normal to the surface corresponds to an energy higher than the surface binding energy. However, for sputtering to happen at all, a minimum projectile kinetic energy is needed. The threshold energy (E_{th}) is the kinetic energy needed for a given projectile and target to induce sputtering.

The target is in our case a meteoroid. The impinging projectiles are the atmospheric constituents. The meteoroid material characteristics needed for sputtering calculations are summarized in Table 1 and are adopted from Tielens et al. (1994) and Öpik (1958). As for the atmospheric constituents, we have used the atoms and molecule number densities given by MSIS-E-90 as described in Section 3.2. Properties of the atmospheric constituents needed to calculate sputtering are summarized in Table 2. Details of the method of calculation follows.

We want to calculate the sputtering yield (Y , the ratio of the mean number of sputtered particles per projectile) at normal incidence on the meteoroid for each atmospheric constituent and find out which of them impinge with energies exceeding the threshold energy. The total yield (Y_{tot}) is the sum of the yields of the projectiles that are energetic enough. Once we have found the sputtering yield, we can calculate the mass loss.

Now to the actual calculations. To begin with, we need to determine the threshold energy E_{th} in eV (Rogers et al., 2005):

$$E_{th} = \begin{cases} 8 E_B \left(\frac{\mu_a}{\mu} \right)^{\frac{1}{3}} & \text{if } \frac{\mu_a}{\mu} > 0.3, \\ \frac{E_B}{\beta(1-\beta)} & \text{if } \frac{\mu_a}{\mu} \leq 0.3, \end{cases} \quad (20)$$

where μ_a (kg) is the projectile mean atomic mass, μ (kg) the mean molecular mass per target atom, and

$$\beta = \frac{4 \mu_a \mu}{(\mu_a + \mu)^2}. \quad (21)$$

Next, a few quantities follow that are to be put into the yield equation (eq. 28). Firstly α , which is a dimensionless, energy independent function of the mass ratio between the target and each projectile (Tielens et al., 1994):

$$\alpha = \begin{cases} 0.3 \left(\frac{\mu}{\mu_a} \right)^{\frac{2}{3}} & \text{if } \frac{\mu}{\mu_a} \geq 0.5, \\ 0.2 & \text{if } \frac{\mu}{\mu_a} < 0.5. \end{cases} \quad (22)$$

Another dimensionless quantity is P , the role of which is to balance α if the ratio $\frac{\mu}{\mu_a}$ grows too big. P is the ratio of the mean projected range to the mean penetrated path length (Rogers et al., 2005):

$$P = \left(K \frac{\mu}{\mu_a} + 1 \right)^{-1}, \quad (23)$$

where K is a dimensionless, truly "free" parameter and depends on the meteoroid material. The values of K for the different materials are given in Table 1. We also need a

variable a (cm), which is essentially the Debye length inside the target and is given by

$$a = \frac{0.0885 r_e}{\sqrt{Z_a^{\frac{2}{3}} + Z^{\frac{2}{3}}}}, \quad (24)$$

where r_e is the classical electron radius in cm. It is important to note that the equations leading to the mass loss due to sputtering are derived in the *cgs* unit system.

The nuclear stopping cross section expressed in the universal relation $s_n(\gamma)$ (ergs m²) can be approximated as (Rogers et al., 2005; Tielens et al., 1994)

$$s_n = \frac{3.441\sqrt{\gamma} \ln(\gamma + 2.718)}{1 + 6.35\sqrt{\gamma} + \gamma(-1.708 + 6.882\sqrt{\gamma})}, \quad (25)$$

where γ is given by

$$\gamma = \frac{\mu}{\mu_a + \mu} \frac{a E}{Z_a Z e^2}. \quad (26)$$

The elementary charge e should be in ergs and also the kinetic energy E with which the impinging molecule hits the target. The kinetic energy is determined from the meteoroid velocity v (m/s):

$$E = \frac{\mu_a v^2}{2} \times 10^7. \quad (27)$$

The sputtering yield calculations are done once for every considered atmospheric constituent colliding with the meteoroid, making seven times. As was discussed earlier, sputtering only occurs when $E > E_{th}$. This means we can exclude the atmospheric atoms and molecules that do not contribute to the sputtering.

The sputtering yield (atoms/projectile) at normal incidence for atoms and molecules causing sputtering is calculated from (Rogers et al., 2005)

$$Y = \frac{3.56}{E_B} \frac{\mu_a}{\mu_a + \mu} \frac{Z_a Z}{\sqrt{Z_a^{\frac{2}{3}} + Z^{\frac{2}{3}}}} \alpha P s_n \left(1 - \left(\frac{E_{th}}{E}\right)^{\frac{2}{3}}\right) \left(1 - \frac{E_{th}}{E}\right)^2, \quad (28)$$

and is valid for $E > E_{th}$. The surface binding energy, E_B , has to be given in eV, whereas the dimensions of E_{th} , E , μ_a and μ do not matter because they cancel each other out. The rest of the parameters are dimensionless.

The total yield (Y_{tot}) from all particles is the sum of the individual yields times their individual number densities (ρ_a):

$$Y_{tot} = \sum_i \rho_{a_i} \cdot Y_i. \quad (29)$$

Finally, the above equations lead us to the mass loss (g/s) equation (Rogers et al., 2005)

$$\text{sputtering} = \left. \frac{dm}{dt} \right|_s = -2 \mu A v \left(\frac{m}{\rho_m}\right)^{\frac{2}{3}} Y_{tot}, \quad (30)$$

where all parameters are given in *cgs* units. The meteoroid mass m is from the previous step in the integration process.

3.5 Flow regime

To determine the meteoroid flow conditions, we calculate the Knudsen number (K_n), a dimensionless ratio between the atmospheric mean free path (l_a) and the characteristic dimension of the meteoroid. Free molecular flow is the regime in which it is enough

to take only collisions with single molecules into account and neglect fluid effects generated by collisions between molecules. This assumption is generally considered to be valid if $K_n > 10$. Since we assume all detected meteoroids to be spheres, their characteristic dimensions are their radii (r_m) (Bronshten, 1983). The Knudsen number is given by

$$K_n = \frac{l_a}{r_m}, \quad (31)$$

but there are several different mean-free-paths near the body that may be defined depending on which atomic particles are considered, and in which frame of reference (Bronshten, 1983). Before ablation of meteoric material has started, and if reflected atmospheric molecules are neglected, the standard atmospheric mean free path (l_∞) may be used. It is defined as

$$l_\infty = \frac{1}{\sqrt{2} \sigma_0 \rho_{a_{tot}}}, \quad (32)$$

where $\sigma_0 = 4.28 \cdot 10^{-19} \text{ m}^{-2}$ is the gas-kinetic cross section of air molecules (Bronshten, 1983) and $\rho_{a_{tot}}$ is the total atmospheric number density at the height of the current step.

The scattering cross section (σ_d) for meteoric atoms and ions on the atmospheric molecules N_2 and O_2 has been found experimentally to depend on meteoroid velocity (v) and may be approximated as (Bronshten, 1983)

$$\sigma_d = 5.6 \cdot 10^{-16.6} \cdot v^{-0.8}, \quad (33)$$

where σ_d is in units of m^2 and v should be given in m/s. The velocity of evaporated molecules (v_e) from the meteoric body is, according to Bronshten (1983),

$$v_e = \sqrt{\frac{8 k_B T}{\pi \mu}}, \quad (34)$$

and their mean free path (l_e) is

$$l_e = \frac{v_e}{\rho_{a_{tot}} v \sigma_d}. \quad (35)$$

Calculating the Knudsen number for evaporated particles at each step in the ablation model it is evident that submillimeter particles are not always in completely free molecular flow conditions. Below an altitude of ~ 100 km, the ratio $\frac{l_e}{r_m}$ is sometimes less than or equal to 10. If this happens, the meteoroid has entered a transition flow regime, which may be described by the theory of first collisions (Bronshten, 1983). The drag coefficient (Γ) and the heat transfer coefficient (Λ) are, in the theory of first collisions, smaller than their free molecular flow values of unity due to the shielding effects of reflected and/or evaporated atomic particles. Preliminary calculations following Bronshten (1979, 1980a,b) show that the shielding effects are small for our simulated meteoroids. At present, shielding effects are therefore not taken into account in the model.

3.6 Deceleration

Travelling through the atmosphere, the meteoroid decelerates due to collisions with the atmospheric constituents. The meteoroid decelerates due to atmospheric drag ($\left. \frac{dv}{dt} \right|_d$), but it also accelerates due to the Earth's gravity. We use the drag equation to calculate deceleration from the conservation of linear momentum:

$$\left. \frac{dv}{dt} \right|_d = - \frac{\Gamma A \rho_a v^2}{m^{\frac{1}{3}} \rho_m^{\frac{2}{3}}}, \quad (36)$$

where ρ_a is the atmospheric mass density and Γ is a dimensionless quantity describing the amount of momentum transferred to the meteoroid by the airflow (Öpik, 1958).

The maximum value it can assume is $\Gamma = 2$, which corresponds to elastic collisions and perfectly-reflected atmospheric molecules. We have adopted $\Gamma = 1$ throughout all calculations, which is the standard assumption in or near free molecular flow.

The acceleration due to the Earth's gravity is expressed as

$$\left. \frac{dv}{dt} \right|_g = \frac{m G M_{\oplus}}{h r_{\oplus}}, \quad (37)$$

where G is the universal gravitational constant, M_{\oplus} is the Earth's mass and r_{\oplus} is the mean Earth radius. The height above the Earth's surface, h , is calculated from the angle θ at the centre of the Earth between the meteor at height h and the common volume. The angle θ is given by the equation:

$$\theta = \tan^{-1} \frac{s \cdot \sin zd}{r_{\oplus} + h_{obs} + s \cdot \cos zd}, \quad (38)$$

where s and zd are the range from the origin and zenith distance, respectively (Section 3.1 and 3.3). The height h is given by:

$$h = \frac{r_{\oplus} + h_{obs} + s \cdot \cos zd}{\cos \theta - r_{\oplus}}. \quad (39)$$

Finally, the total meteoroid deceleration is

$$\frac{dv}{dt} = \left. \frac{dv}{dt} \right|_d + \left. \frac{dv}{dt} \right|_g. \quad (40)$$

3.7 Meteoroid temperature

The heat transfer coefficient (Λ) determines the convection heat transfer between a moving fluid and a solid body (Bronshten, 1983). It is equal to unity if the total kinetic energy of atmospheric constituents colliding with a meteoroid goes into ablation. According to Öpik (1958), $\Lambda \simeq 1$ for a particle in free molecular flow if vaporization is the primary ablation mechanism.

Friichtenicht and Becker (1973) have done perhaps the most advanced laboratory experiments to determine Λ . Microparticles were charged, injected into and accelerated in a 2 MV Van de Graaff accelerator tube and guided through an analysis region with time-of-flight and charge detectors. To achieve free molecular flow conditions at meteoric velocities and still have a meteor trail length contained in a reasonable laboratory apparatus, Friichtenicht and Becker (1973) injected submicron sized particles of various materials such as iron, iron metatitanate (FeTiO_3), nickel aluminide (NiAl) and silicon etc. and let them enter a gas target of variable pressure surrounded by photomultiplier tubes. The heat transfer coefficient was found to decrease linearly from about 0.8 at 25 km/s to 0.4 at 40 km/s. In fitting the model to the data, we have used different fixed values of Λ : 0.2, 0.4, 0.6, 0.8 and 1.0 to see which fit best. It is likely that Λ in reality is not constant along a meteoroid trajectory (Campbell-Brown and Koschny, 2004).

To obtain the rate of change of temperature of the meteoroid ($\frac{dT}{dt}$), we need to make certain assumptions. We assume a homogeneous meteoroid experiencing an isotropic flux and that the meteoroid undergoes isothermal heating. Then the heat balance equation per cross-sectional area is given by (Hill et al., 2005)

$$\frac{\Lambda \rho_a v^3}{2} = 4 k_B \epsilon (T^4 - T_a^4) + \frac{C m^{\frac{1}{3}} \rho_m^{\frac{2}{3}}}{A} \frac{dT}{dt} - \frac{L}{A} \left(\frac{\rho_m}{m} \right)^{\frac{2}{3}} \left. \frac{dm}{dt} \right|_{th}, \quad (41)$$

where

k_B	= Stefan-Boltzmann constant	= $5.67 \times 10^{-8} \text{ W}/(\text{m}^2\text{K}^4)$,
ϵ	= emissivity	= 0.9,
T_a	= effective atmospheric temperature	= 280 K,
C	= specific heat of meteoroid	= 1200 J/(Kkg),
L	= latent heat of fusion + vaporization	= $6.0 \times 10^6 \text{ J/kg}$.

The variables v , m , T and $\left.\frac{dm}{dt}\right|_{th}$ are the meteoroid velocity, mass, temperature and mass loss due to thermal ablation respectively, as calculated in the previous step of the integration. Solving for $\left.\frac{dT}{dt}\right|_{th}$ we get

$$\left.\frac{dT}{dt}\right|_{th} = \frac{A}{C m^{\frac{1}{3}} \rho_m^{\frac{2}{3}}} \left(\frac{\Lambda \rho_a v^3}{2} - 4 k_B \epsilon (T^4 - T_a^4) + \frac{L}{A} \left(\frac{\rho_m}{m} \right)^{\frac{2}{3}} \left.\frac{dm}{dt}\right|_{th} \right). \quad (42)$$

3.8 Radar cross section

We are well aware that the overdense assumption described in Section 2.7 provides an oversimplified picture of the true physical conditions of the scattering process, but we have still used it as a first-order approach to compare the measured RCS with the ablation model, following previous work by Close et al. (2002) and Westman et al. (2004). The overdense assumption has also been used by Bass et al. (2008) in a similar comparison of RCS with an ablation model as is described here.

The scattering cross section σ_d for meteoric atoms and ions on atmospheric N_2 and O_2 molecules and the velocity of atoms evaporated from the meteoric body (v_e) have been discussed in Section 3.5. The mean free path of the evaporated atoms (l_e) is the average distance travelled by an atom between collisions. More specifically, it is the range at which a fraction $1 - 1/e \simeq 0.77$ of the evaporated atoms have already collided with air molecules.

An estimate of the probability (β_0) that primary collisions lead to ionization (Jones, 1997) is

$$\beta_0 = \frac{c \cdot (v - v_0)^2 \cdot v^{0.8}}{1 + c \cdot (v - v_0)^2 \cdot v^{0.8}}, \quad (43)$$

where c is an empirically-derived coefficient and v_0 is the minimum velocity at which ionization can take place. Values for some elements assumed to be present in the composition of a cometary meteoroid are summarized in Table 3, adopted from Jones (1997).

As a very crude estimation of the plasma in the immediate vicinity of the meteoroid, we let the meteoroid be a source of atoms where the rate of evaporated atoms per unit of time is estimated at each step of the ablation model. These atoms expand radially from the meteoroid with the thermal velocity (v_e). The number of electrons in a spherical shell at a specific range from the meteoroid is estimated by the primary ionization probability (β_0) times the number of collided atoms at that range. We assume furthermore a non-collisional expansion of the electrons. The size of the radar target is calculated as the range (r_{od}) from the centre of the meteoroid where the density of the

Table 3: Ionization parameters for elements assumed to be present in the composition of a cometary meteoroid (Jones, 1997). Assumed percentage composition by weight (%), proportion by atom number (p), minimum velocity at which ionization takes place (v_0), empirically derived coefficient (c) and ratio of atom mass to a nitrogen molecule (μ_r).

Element	%	p	v_0 (km/s)	c	μ_r
O	45	0.617	16.7	$4.66 \cdot 10^{-6}$	0.57
Fe	15	0.059	9.4	$34.50 \cdot 10^{-6}$	2.0
Mg	9	0.082	11.1	$9.29 \cdot 10^{-6}$	0.86
Si	31	0.242	11.0	$18.50 \cdot 10^{-6}$	1.0

plasma drops below the critical density. The highest altitude at which the plasma density in the vicinity of the meteoroid exceeds critical was investigated by Westman et al. (2004) and depends on the mass and velocity of the meteoroid. It also depends on the assumed heat transfer coefficient and meteoroid density.

The remainder of this section describes the method used to calculate the RCS of a perfectly-conducting sphere of radius r_{od} following Blake (1991):

$$\frac{\sigma}{\pi r_{od}^2} = \frac{1}{x^2} \left| \sum_{n=1}^{\infty} (-1)^n (2n+1) (C_n + D_n) \right|^2, \quad (44)$$

where σ is the RCS. The quantity x is dependent on the radar wavelength λ and is given by

$$x = \frac{2\pi r_{od}}{\lambda} \quad (45)$$

For a perfectly conducting sphere C_n and D_n are calculated as

$$C_n = \frac{j_n(x)}{h_n^{(2)}(x)}, \quad (46)$$

$$D_n = \frac{-\frac{d}{dx}(x j_n(x))}{\frac{d}{dx}(x h_n^{(2)}(x))}, \quad (47)$$

where j_n and $h_n^{(2)}$ are the spherical Bessel functions of the first kind and the spherical Hankel functions of the second kind respectively. They are defined as

$$j_n \equiv \sqrt{\frac{\pi}{2x}} J_{n+\frac{1}{2}}(x), \quad (48)$$

where $J_{n+\frac{1}{2}}$ is the Bessel function of the first kind, and as

$$h_n^{(2)} \equiv \sqrt{\frac{\pi}{2x}} H_{n+\frac{1}{2}}^{(2)}(x), \quad (49)$$

where $H_{n+\frac{1}{2}}^{(2)}$ is the Hankel function of the second kind. The derivatives of j_n and $h_n^{(2)}$ are defined as

$$\frac{d}{dx}(j_n(x)) = \frac{1}{2} \left(j_{n-1}(x) - \frac{j_n(x) + x j_{n+1}(x)}{x} \right), \quad (50)$$

$$\frac{d}{dx}(h_n^{(2)}(x)) = \frac{1}{2} \left(h_{n-1}^{(2)}(x) - \frac{h_n^{(2)}(x) + x h_{n+1}^{(2)}(x)}{x} \right). \quad (51)$$

3.9 Output parameters

The output parameters determined at each step in the Runge-Kutta integration technique are meteoroid velocity (v), mass (m), temperature (T) and range (s) (Section 3.3). Other output parameters are a matter of choice and have to be determined after the integration has taken place.

Additional parameters that are calculated and provided to the user for each integrated meteoroid are the step size in seconds and the cumulative time from start, the height (h) above the Earth surface, the angle (θ) at the centre of the Earth between the meteor at height h and the common volume, the meteoroid radius (r_m), meteoroid mass

loss due to ablation ($\left.\frac{dm}{dt}\right|_{th}$) and sputtering ($\left.\frac{dm}{dt}\right|_s$), and luminous intensity (Szasz et al., 2008b).

The above-atmosphere velocity, together with zenith distance and azimuth of the velocity vector are used as input to a function to calculate the orbital elements and ecliptic radiants of the trisstatic particles. Szasz et al. (2008a) present these astronomical results and Szasz (2008) describes the method in detail.

3.10 Fit of the model to the data

This section describes how the output from the ablation model is fitted to the data by varying the input parameters.

The automated fit function runs through all four meteoroid densities (ρ_m) paired with all five heat transfer coefficients (Λ). However, we have to begin and stop somewhere. Before the first run with a new density, a best guess has to be made for the input parameters. Since the meteoroid decelerates when travelling through the atmosphere, its velocity above the atmosphere is as an initial guess set at 5% larger than the observed meteoroid velocity. We use the measured meteoroid trajectory zenith distance (zd) as input as well as an initial guess of the atmospheric entry mass (m_{start}) depending on meteoroid density:

$$m_{start} = \begin{cases} 10^{-6}\text{kg} & \text{if } \rho_m = 0.3 \text{ g/cc,} \\ 10^{-7}\text{kg} & \text{if } \rho_m = 1.0 \vee 3.3 \text{ g/cc,} \\ 10^{-8}\text{kg} & \text{if } \rho_m = 7.8 \text{ g/cc.} \end{cases} \quad (52)$$

The starting assumptions have been chosen empirically to keep the number of iterations down. After each run, the new deceleration and radius is compared to the data and the function varies the starting parameters considering the difference between the two values as well as the previous starting parameters before running the model again.

The restrictions on where to terminate the integration is set to when the mass has decreased to $stop_m=10^{-4} \times$ the original mass, the particle has reached to an altitude of $stop_h=85$ km, the velocity has decelerated to $stop_v=10$ km/s, or a maximum number of 300 steps has been reached.

After each integration down through the atmosphere, the simulated target size according to Rayleigh scattering is calculated. Then a function is fitted to both the modelled velocity and the target radius and their values are compared to the measured ones at each and every data point. A leap (not to be mixed up with the steps in the integration through the atmosphere) is then taken in mass and velocity and new values are obtained with the ablation model.

If the model particle does not reach down to the observing altitude, the initial mass has to be increased. If the model values jump from one side of the observed curve to the other, or if no minimum seems to be found, the leap size has to be decreased. If the maximum of the model target radius is below the observed target cross section, the meteoroid mass has to be decreased. It is also important to keep track of differences from leap to leap, because if for example the algorithm is increasing the initial mass but the difference in target radius only grows for each run, the mass has to be decreased instead to make the model fit the data better. When the fit cannot be improved any more, the iteration is ended and the next meteoroid density is tried instead. The fit is satisfactory when the mean least-square error in velocity is smaller than 10 m/s and the target residuals do not improve, or the initial mass needs to be decreased further but cannot because, e.g., the meteoroid in this case ablates completely above the measurement altitude. It is not at all certain that all densities and all heat transfer coefficients can be made to fit the data. Therefore, a maximum number of 30 iterations are allowed.

The results from all iterations for one and the same meteoroid are saved and compared at a later stage.

To compare the fits with different densities and heat transfer coefficients for one and the same meteoroid, we have defined a figure of merit (\mathcal{Q}). As a first step, we calculate the error in the result for each point in both velocity (e_v) and radius (e_r). We also weight each point in proportion to its pulse compression squared (see Paper I and VI). The weight (w_i) of each data point (i) is an estimate of its accuracy; the higher the weight, the more accurate it is. A combination of two slightly different parameters (\mathcal{Q}_{100} and \mathcal{Q}_{1000}) have proven empirically to give a reliable figure of merit:

$$\mathcal{Q}_{100} = \sum_i w_i^2 \left[\left(\frac{e_{v_i}}{100} \right)^2 + \left(\frac{e_{r_i}}{100} \right)^2 \right], \quad (53)$$

$$\mathcal{Q}_{1000} = \sum_i w_i^2 \left[\left(\frac{e_{v_i}}{100} \right)^2 + \left(\frac{e_{r_i}}{1000} \right)^2 \right], \quad (54)$$

$$\mathcal{Q} = \mathcal{Q}_{100} + \mathcal{Q}_{1000}. \quad (55)$$

$$(56)$$

The fit with the lowest \mathcal{Q} number is the best one, and hence is chosen. The parameters of the best fit are used as characteristics of the fitted meteoroid to calculate its orbit (Szasz et al., 2008a) and estimate its visual magnitude (Szasz et al., 2008b), to name two examples. The mass distribution of the meteoroids is reported in Paper I.

There is a tendency for higher velocity meteoroids to fit better with a lower heat transfer coefficient, consistent with the laboratory experiments by Friichtenicht and Becker (1973). In Figure 6a the arithmetic of the mean meteoroid velocity within the common volume (\bar{v}_{cv}) is plotted for each value of the heat transfer coefficient. The vertical bars show the standard deviations. There is also a trend in the mean velocity for different density values – lower velocity particles being better fitted with lower density – displayed in Figure 6b. The latter trend is probably not a sign of low geocentric velocity meteoroids in general having lower density than high geocentric velocity meteoroids. It may, however, be a selection effect of the limited altitude interval monitored during the measurement campaigns (see further details in Paper I) and hence a sign that particles of low density and high geocentric velocity do not survive down to 96 km (Szasz et al., 2008a). It may also be an artifact produced by the modelling assumptions.

Figure 7a and Table 4 report the distribution of the number of meteoroids for each combination of best-fitted meteoroid density and heat transfer coefficient. Figure 7b shows \bar{v}_{cv} for each combination. There are clear trends of higher \bar{v}_{cv} with increasing density for each value of the heat transfer coefficient, as well as higher \bar{v}_{cv} with decreasing heat transfer coefficient for each value of the density.

		ρ_m (g/cc)			
		0.3	1.0	3.3	7.8
Λ	0.2	2	26	65	15
	0.4	5	18	72	31
	0.6	2	12	23	27
	0.8	2	9	13	19
	1.0	5	18	28	18

Table 4: Number of meteoroids for each combination of meteoroid density (ρ_m) and heat transfer coefficient (Λ). The total number of meteoroids is 410.

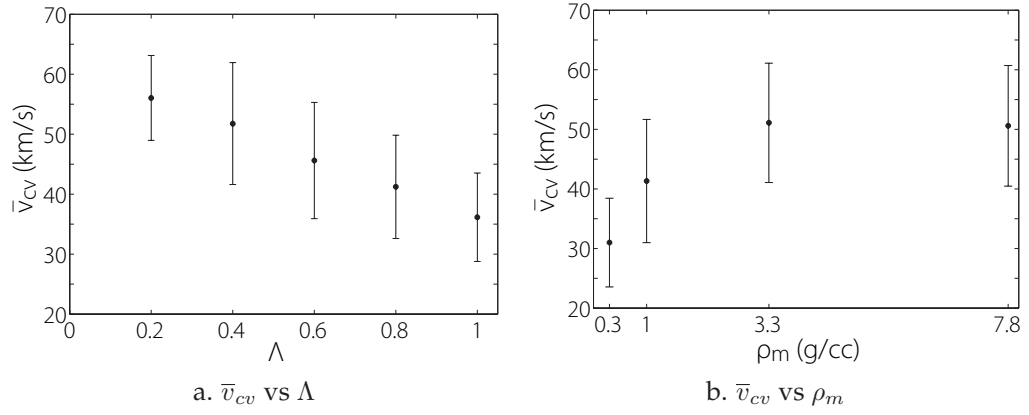


Figure 6: The arithmetic mean of the meteoroid velocity within the common volume (\bar{v}_{cv}) versus a) each value of heat transfer coefficient (Λ), and b) meteoroid density (ρ_m). The vertical bars show standard deviations.

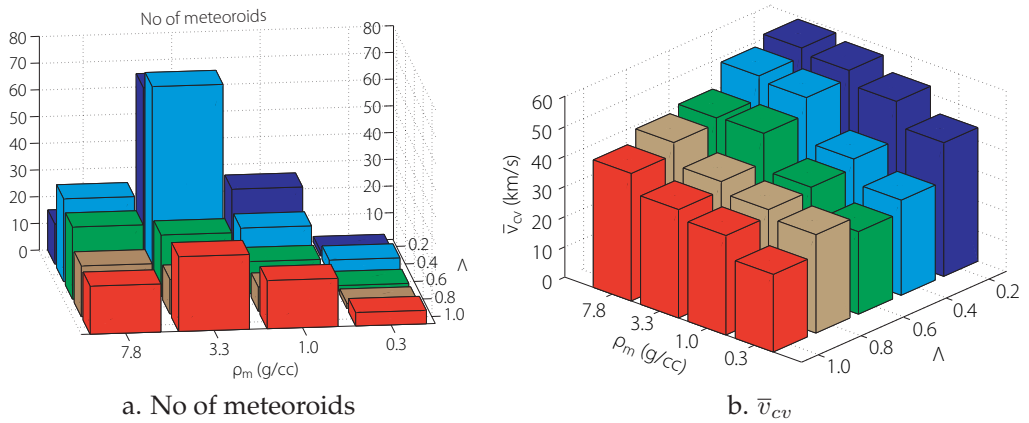


Figure 7: a) Number of meteoroids, and b) the arithmetic mean of the meteoroid velocity within the common volume (\bar{v}_{cv}) for each combination of meteoroid density (ρ_m) and heat transfer coefficient (Λ).

4 SUMMARY OF THE INCLUDED PAPERS

4.1 Paper I: Determination of meteoroid physical properties from tristatic radar observations

Paper I reviews the meteor head echo observations carried out with the tristatic 930 MHz EISCAT UHF radar system during four 24 h runs between 2002 and 2005 and compare them with earlier observations. A total number of 410 tristatic meteors were observed. The velocities of the detected meteoroids are in the range 19–70 km/s, but with very few detections below 30 km/s. The estimated masses are in the range 10^{-9} – $10^{-5.5}$ kg.

The paper presents a method for determining the position of a compact radar target in the common volume is presented and demonstrates its applicability for meteor studies. It also describes how the inferred positions of the meteor targets are utilized to estimate their velocities, decelerations and directions of arrival as well as their radar cross sections with unprecedented accuracy.

It furthermore demonstrates that the effect of finite beamwidth leads to a radial deceleration that is larger than the true deceleration for an approaching meteoroid. The radial velocity is, however, always smaller than the true velocity. Monostatic radar observations conducted with a vertically pointed beam often use radial deceleration and radial velocity as estimates of the true quantities in a momentum equation of motion, but these therefore underestimate the meteoroid masses.

4.2 Paper II: On the meteoric head echo radar cross section angular dependence

Paper II presents radar cross section (RCS) measurements of meteor head echoes observed with the EISCAT UHF system. The geographical configuration of the three receivers has been exploited such that the common volume of the antenna beams was simultaneously viewed from disparate angles, offering a unique possibility to compare the monostatic RCS of a meteor target accurately with two simultaneously-probed bistatic RCSs. We conclude that the head echoes observed with the EISCAT UHF system are detected at virtually all possible aspect angles all the way out to 130° from the meteoroid trajectory, limited by the antenna pointing directions. The RCS of individual meteors as observed by the three receivers are equal within the accuracy of the measurements. The ratios of the RCS measured at the different receivers show a slight trend with respect to aspect angle, the trend suggesting that the RCS may decrease at a rate of 0.2 dB per 10° with increasing aspect angle.

4.3 Paper III: Three dimensional radar observation of a submillimeter meteoroid fragmentation

Paper III discusses two examples of pulsating meteor events observed with the EISCAT UHF radar system. One of them provides the first strong observational evidence of a submillimeter-sized meteoroid breaking apart into two distinct fragments. The received power fluctuates regularly but with different frequencies in the time profiles of all three receivers. We argue that the pulsations are generated by interference between radio wave reflections from more than one distinct ionized region due to two meteoroid fragments simultaneously present in the transmitter radar beam. The result is consistent with interference from two fragments of unequal cross-sectional area over mass ratio separating from each other due to different deceleration along the trajectory of their parent meteoroid. The slightly-unequal velocities of the fragments with respect to each other and the receivers produce diverse interference patterns at all three receivers.

The other meteor event investigated in Paper III is an example of a meteoroid undergoing quasi-continuous disintegration. This manifests itself as simultaneous pulsations at all three receivers. Both observations indicate a head echo target upper size limit of the order of half the 32 cm radar wavelength.

The paper confirms that it is possible to study the fragmentation processes of very small meteoroids by investigating the characteristics of radar power profiles. This discovery promises to be useful in the further understanding of the interaction processes of meteoroids with the Earth's atmosphere and thus also the properties of interplanetary/interstellar dust.

4.4 Paper IV: Power fluctuations in meteor head echoes observed with the EISCAT VHF radar

Paper IV presents preliminary results from a 6 h meteor experiment carried out with the 224 MHz EISCAT VHF radar in Tromsø, Norway, on November 26, 2003, and discusses echoes containing pulsations in the frequency range 20-200 Hz. When Paper IV was written, the process causing the echo power pulsations had not yet been identified. Paper IV gives plasma effects as the most likely cause, or rotating asymmetrical dust grains causing a modulation of the ionization rate.

Later experiments on the tristatic EISCAT UHF system showed the same features in received power and Paper III reported that some of them are caused by meteoroid fragmentation. Pulsations may also be caused by plasma resonance effects as demonstrated by Dyrud et al. (2008) and discussed in Section 2.8.

4.5 Paper V: Properties of the meteor head echoes observed with the EISCAT radars

Paper V contains a statistical study of pulsating VHF echoes recorded during the 6 h observation on November 26, 2003, with the 224 MHz EISCAT VHF radar and an example of a tristatic pulsating event detected at winter solstice 2004 with the 930 MHz EISCAT UHF radar system.

The majority of the 2500 meteor head echoes observed with the EISCAT VHF radar do not have smooth power profiles, which would be the case for a constant cross section target convolved with the main lobe of the antenna beam pattern. Neither the altitude distribution, the signal-to-noise ratio distribution nor the line-of-sight velocity distribution of pulsating events differ from the distributions of non-pulsating events.

It is concluded that some of the pulsating events may be due to interference from ionized regions caused by meteoric fragments simultaneously present in the radar beam.

4.6 Paper VI: The EISCAT meteor code

Paper VI reports the development and particulars of the radar measurement coding technique used in the meteor observations presented in Papers I to V. The pulse coding and decoding scheme which is described was invented by my coauthors Wannberg and Westman. The transmitter carrier is modulated with a low-sidelobe 32-bit binary phase shift keyed (BPSK) sequence having $2.4 \mu\text{s}$ baudlength, giving a total pulse length of $76.8 \mu\text{s}$. The transmitted code is oversampled by a factor of four with a $0.6 \mu\text{s}$ sampling period in the receiver data stream, corresponding to 90 m range resolution. Target range and Doppler velocity are extracted from the raw data in a multi-step matched-filter procedure.

Paper VI also contains a statistical evaluation of the accuracy of the meteor target Doppler velocity determination procedure, as well as a case study of the possibility to resolve adjacent multiple targets, both carried out by me and my coauthor Szasz. We show that the determined Doppler velocity agrees with the target range rate to about one part in 1000 with negligible biases. This demonstrates that no contribution from slipping plasma is detected and that the Doppler velocities are unbiased within the measurement accuracy. Two targets can be discriminated if they are separated by more than ~ 100 m. The multiple targets are independent meteoroids passing through the radar beam at the same time and are not caused by fragmentation of one meteoroid in the atmosphere.

ACKNOWLEDGEMENTS

TILLKÄNNAGIVANDEN

De uppgifter en doktorand ställs inför kan liknas vid att lämnas ensam, utan karta och kompass, till fots i väglös terräng. I Kiruna är den väglösa terrängen kanske mer vidsträckt och svårframkomlig än på många andra ställen, men å andra sidan är ofta sikten god och utsikten väl värd besväret. Asta Pellinen-Wannberg har uppmuntrat mig att trampa egna stigar, röjt hinder ur vägen och sammanfört mig med många vägvisare. Tack Asta!

I have had the opportunity to discuss meteor science with many great scientists. David Meisel and Edmond Murad distinguish themselves by the enthusiasm with which they both communicate their substantial knowledge and experience. Dave, I will always remember the term spent as a guest at SUNY Geneseo with warmth!

Gudmund Wannberg, Assar Westman och Ingemar Häggström har på olika sätt hjälpt mig att förstå EISCAT:s radarsystem, mätteknikens grundprinciper och dataanalysmetoder. Under de flertalet radarexperiment som avhandlingen bygger på har jag haft stor hjälp av personalen vid EISCAT:s tre fastlandstationer. Urban Brändström har genom tålmodiga insatser under våra försök att observera meteoriter med ALIS lärt mig mycket om optiska mätningar och fjärrstyrda instrument. Det har varit väldigt givande Urban!

Många vid IRF i Kiruna har bidragit till att göra min doktorandtid minnesvärd: ingen nämnd, men ingen glömd. Tack också till den nationella forskarskolan i rymdteknik för att tillsammans med IRF ha finansierat min forskning. Familj, vänner och framförallt **Csilla** utgör grunden i den trygga bas som möjliggjort avhandlingsarbetet.

REFERENCES

- Appleton, E. V., Naismith, R., and Ingram, L. J. (1937). British radio observations during the Second International Polar Year 1932-33. *Philosophical Transactions of the Royal Society of London. Series A, Mathematical and Physical Sciences*, 236(764):191–259.
- Baggaley, W. J., Bennett, R. G. T., Steel, D. I., and Taylor, A. D. (1994). The Advanced Meteor Orbit Radar facility - AMOR. *Quarterly Journal of the Royal Astronomical Society*, 35:293–320.
- Bass, E., Oppenheim, M., Chau, J., and Olmstead, A. (2008). Improving the accuracy of meteoroid mass estimates from head echo deceleration. *Earth, Moon, and Planets*, 102:379–382.
- Beech, M. and Steel, D. (1995). On the definition of the term ‘meteoroid’. *Quarterly Journal of the Royal Astronomical Society*, 36:281–284.
- Billam, E. R. and Browne, I. C. (1956). Characteristics of radio echoes from meteor trails IV: Polarization effects. *Proceedings of the Physical Society B*, 69:98–113.
- Blackett, P. M. S. and Lovell, A. C. B. (1941). Radio echoes and cosmic ray showers. *Royal Society of London Proceedings Series A*, 177:183–186.
- Blake, L. V. (1991). *Radar range-performance analysis*. Munro Publishing Co., Silver Spring, MD, USA.
- Bronshten, V. A. (1979). Effects of the shielding of the surface of a meteoroid by vaporized and reflected molecules. I - Application of the theory of first collisions. *Astronomicheskii Vestnik*, 13:99–105.
- Bronshten, V. A. (1980a). Effects of shielding the surface of a meteoroid by molecules that are flying off and evaporating. II - Shielding under conditions of the start of intense evaporation. *Astronomicheskii Vestnik*, 13:169–177.
- Bronshten, V. A. (1980b). Shielding effects of a meteoroid surface by reflecting and evaporating molecules. III - The case of strong shielding - the overall picture of the phenomenon. *Astronomicheskii Vestnik*, 13:224–231.
- Bronshten, V. A. (1983). *Physics of meteoric phenomena*. D. Reidel Publishing Company.
- Brownlee, D. E. (1985). Cosmic dust: collection and research. *Annual Review of Earth and Planetary Physics*, 13:147–173.
- Butrica, A. J. (1996). *To see the unseen: a history of planetary radar astronomy*. The NASA history series. Washington, DC : National Aeronautics and Space Administration.
- Campbell-Brown, M. D. and Koschny, D. (2004). Model of the ablation of faint meteors. *Astronomy & Astrophysics*, 418:751–758.
- Ceplecha, Z., Borovička, J., Elford, W. G., ReVelle, D. O., Hawkes, R. L., Porubčan, V., and Šimek, M. (1998). Meteor phenomena and bodies. *Space Science Reviews*, 84:327–471.
- Chau, J. L. and Woodman, R. F. (2004). Observations of meteor-head echoes using the Jicamarca 50 MHz radar in interferometer mode. *Atmospheric Chemistry & Physics*, 4:511–521.
- Clegg, J. A. and Closs, R. L. (1951). Letters to the editor: Plasma oscillations in meteor trails. *Proceedings of the Physical Society B*, 64:718–719.

- Close, S. (2004). *Theory and analysis of meteor head echoes and meteoroids using high-resolution multi-frequency radar data*. PhD thesis, Boston University.
- Close, S., Brown, P., Campbell-Brown, M., Oppenheim, M., and Colestock, P. (2007). Meteor head echo radar data: Mass velocity selection effects. *Icarus*, 186:547–556.
- Close, S., Hunt, S. M., Minardi, M. J., and McKeen, F. M. (2000). Analysis of Perseid meteor head echo data collected using the Advanced Research Projects Agency Long-Range Tracking and Instrumentation Radar (ALTAIR). *RS*, 35:1233–1240.
- Close, S., Oppenheim, M., Hunt, S., and Coster, A. (2004). A technique for calculating meteor plasma density and meteoroid mass from radar head echo scattering. *Icarus*, 168:43–52.
- Close, S., Oppenheim, M., Hunt, S., and Dyrud, L. (2002). Scattering characteristics of high-resolution meteor head echoes detected at multiple frequencies. *Journal of Geophysical Research (Space Physics)*, 107:9–1.
- Cook, A. F. I., Flannery, M. R., Levy, H. I., McCrosky, R. E., Sekanina, Z., Shao, C., Southworth, R. B., and Williams, J. T. (1972). Meteor research program. NASA Contractor Report NASA-CR-2109, Smithsonian Institute, Cambridge MA.
- Danby, J. M. A. (1988). *Fundamentals of celestial mechanics*. Willmann-Bell, 2nd. rev. and enlarged edition.
- Dyrud, L., Wilson, D., Boerve, S., Trulsen, J., Pecseli, H., Close, S., Chen, C., and Lee, Y. (2007). Plasma and electromagnetic wave simulations of meteors. *Advances in Space Research*. doi:10.1016/j.asr.2007.03.048.
- Dyrud, L., Wilson, D., Boerve, S., Trulsen, J., Pecseli, H., Close, S., Chen, C., and Lee, Y. (2008). Plasma and electromagnetic simulations of meteor head echo radar reflections. *Earth, Moon, and Planets*, 102:383–394.
- Eckersley, T. L. (1937). Irregular ionic clouds in the E layer of the ionosphere. *Nature*, 139:846–847.
- Evans, J. V. (1965). Radio-echo studies of meteors at 68-centimeter wavelength. *Journal of Geophysical Research*, 70:5395–5416.
- Evans, J. V. (1966). Radar observations of meteor deceleration. *Journal of Geophysical Research*, 71:171–188.
- Friichtenicht, J. F. and Becker, D. G. (1973). Determination of meteor parameters using laboratory simulation techniques. *NASA Special Publication*, 319:53–81.
- Galligan, D. P. and Baggaley, W. J. (2004). The orbital distribution of radar-detected meteoroids of the solar system dust cloud. *Monthly Notices of the Royal Astronomical Society*, 353:422–446.
- Greenhow, J. S. and Neufeld, E. L. (1956). Phase changes and resonance effects in radio echoes from meteor trails. *Proceedings of the Physical Society B*, 69:1069–1076.
- Hawkes, R. L., P., B., and Mann, I., editors (2005). *Modern meteor science: an interdisciplinary view*. Springer, Dordrecht, The Netherlands.
- Hedin, A. E. (1991). Extension of the MSIS thermosphere model into the middle and lower atmosphere. *Journal of Geophysical Research*, 96:1159–1172.
- Herlofson, N. (1951). Plasma resonance in ionospheric irregularities. *Arkiv för fysik*, 3(15):247–297.

- Hey, J. S., Parsons, S. J., and Stewart, G. S. (1947). Radar observations of the Giacobinids meteor shower, 1946. *Monthly Notices of the Royal Astronomical Society*, 107:176–183.
- Hey, J. S. and Stewart, G. S. (1946). Derivation of meteor stream radiants by radio reflection methods. *Nature*, 158(4014):481–482.
- Hill, K. A., Rogers, L. A., and Hawkes, R. L. (2004). Sputtering and high altitude meteors. *Earth Moon and Planets*, 95:403–412.
- Hill, K. A., Rogers, L. A., and Hawkes, R. L. (2005). High geocentric velocity meteor ablation. *Astronomy & Astrophysics*, 444:615–624.
- Hocking, W. K., Fuller, B., and Vandeppeer, B. (2001). Real-time determination of meteor-related parameters utilizing modern digital technology. *Journal of Atmospheric and Solar-Terrestrial Physics*, 63:155–169.
- Janches, D., Heinselman, C. J., Chau, J. L., Chandran, A., and Woodman, R. (2006). Modeling the global micrometeor input function in the upper atmosphere observed by high power and large aperture radars. *Journal of Geophysical Research (Space Physics)*, 111(A10):A07317.
- Janches, D., Meisel, D. D., and Mathews, J. D. (2001). Orbital properties of the Arecibo micrometeoroids at Earth interception. *Icarus*, 150:206–218.
- Jones, J., Brown, P., Ellis, K. J., Webster, A. R., Campbell-Brown, M., Krzeminski, Z., and Weryk, R. J. (2005). The Canadian Meteor Orbit Radar: System overview and preliminary results. *Planetary and Space Science*, 53:413–421.
- Jones, J. and Webster, A. R. (1991). Visual and radar studies of meteor head echoes. *Planetary and Space Science*, 39:873–878.
- Jones, W. (1997). Theoretical and observational determinations of the ionization coefficient of meteors. *Monthly Notices of the Royal Astronomical Society*, 288:995–1003.
- Kaiser, T. R., editor (1955). *Meteors*. Pergamon Press Ltd., London and New York.
- Love, S. G. and Brownlee, D. E. (1991). Heating and thermal transformation of micrometeoroids entering the Earth's atmosphere. *Icarus*, 89:26–43.
- Lovell, A. C. B. (1947). Electron density in meteor trails. *Nature*, 160(4072):670–671.
- Lovell, A. C. B. and Clegg, J. A. (1948). Characteristics of radio echoes from meteor trails: I. The intensity of the radio reflections and electron density in the trails. *Proceedings of the Physical Society*, 60:491–498.
- Manning, L. A. (1958). The initial radius of meteoric ionization trails. *Journal of Geophysical Research*, 63:181–196.
- Mathews, J. D. (2004). Radio science issues surrounding HF/VHF/UHF radar meteor studies. *Journal of Atmospheric and Terrestrial Physics*, 66:285–299.
- Mathews, J. D., Briczinski, S. J., Meisel, D. D., and Heinselman, C. J. (2008). Radio and meteor science outcomes from comparisons of meteor radar observations at AMISR Poker Flat, Sondrestrom and Arecibo. *Earth, Moon, and Planets*, 102:365–372.
- Mathews, J. D., Meisel, D. D., Hunter, K. P., Getman, V. S., and Zhou, Q. (1997). Very high resolution studies of micrometeors using the Arecibo 430 MHz radar. *Icarus*, 126:157–169.
- McIntosh, B. A. (1963). Experimental study of the amplitude of radar meteor-head echoes. *Canadian Journal of Physics*, 41:355–371.

- McKinley, D. W. R. (1961). *Meteor science and engineering*. McGraw-Hill Series in Engineering Sciences. McGraw-Hill Book Company, Inc.
- McKinley, D. W. R. and Millman, P. M. (1949). A phenomenological theory of radar echoes from meteors. *Proceedings of the IRE*, 37(4):364–375.
- McSween, H. Y. (1999). *Meteorites and their parent planets*. Cambridge University Press, 2nd edition.
- Millman, P. M. (1961). Meteor news. *Journal of the Royal Astronomical Society of Canada*, 55:265–268.
- Millman, P. M., McKinley, D. W. R., and Burland, M. S. (1947). Combined radar, photographic and visual observations of the Perseid meteor shower of 1947. *Nature*, 161(4086):278–280.
- Murad, E. and Williams, I. P. (2002). *Meteors in the Earth's atmosphere*. Cambridge University Press, Cambridge, UK.
- Nagaoka, H. (1929). Possibility of disturbance of radio transmissions by meteoric showers. *Proceedings of the Imperial Academy, Tokyo*, 5:233.
- Öpik, E. J. (1958). *Physics of meteor flight in the atmosphere*. Number 6 in Interscience tracts on physics and astronomy. Interscience Publishers, Inc.
- Pedrotti, F. L. and Pedrotti, L. S. (1996). *Introduction to optics*. Prentice-Hall International, 2nd edition.
- Pellinen-Wannberg, A. and Wannberg, G. (1994). Meteor observations with the European Incoherent Scatter UHF radar. *Journal of Geophysical Research*, 99(A6):11379–11390.
- Pellinen-Wannberg, A., Westman, A., Wannberg, G., and Kaila, K. (1998). Meteor fluxes and visual magnitudes from EISCAT radar event rates: a comparison with cross-section based magnitude estimates and optical data. *Annales Geophysicae*, 16:1475–1485.
- Pierce, J. A. (1938). Abnormal ionization in the E region atmosphere. *Proc. Inst. Radio Eng.*, 26:892–908.
- Poynting, J. H. (1903). Radiation in the solar system: its effect on temperature and its pressure on small bodies. *Proceedings of the Royal Society*, 72:265–267.
- Rietmeijer, F. J. M. (2002). The earliest chemical dust evolution in the solar nebula. *Chemie der Erde*, 62:1–45.
- Robertson, H. P. (1937). Dynamical effects of radiation in the solar system. *Monthly Notices of the Royal Astronomical Society*, 97:423–438.
- Rogers, L. A., Hill, K. A., and Hawkes, R. L. (2005). Mass loss due to sputtering and thermal processes in meteoroid ablation. *Planetary and Space Science*, 53:1341–1354.
- Sato, T., Nakamura, T., and Nishimura, K. (2000). Orbit determination of meteors using the MU radar. *IEICE TRANSACTIONS on Communications*, E83-B(9):1990–1995.
- Skellett, A. M. (1931). The effect of meteors on radio transmission through the Kennelly-Heaviside layer. *Physical Review*, 37:1668–1668.
- Skellett, A. M. (1938). Meteoric ionization in the E region of the ionosphere. *Nature*, 141:472.

